J. Mech. Phys. Solids 190 (2024) 105694

Contents lists available at ScienceDirect

Journal of the Mechanics and Physics of Solids

journal homepage: www.elsevier.com/locate/jmps

A variational phase-field framework for multiphysics modelling of degradation and stress corrosion cracking in biodegradable magnesium alloys

Dawei Zhang [a], Songyun Ma [a,*], Julia Nachtsheim [a], Shunqi Zhang [b], Bernd Markert [a]

[a] Institute of General Mechanics, RWTH Aachen University, Aachen, Germany
[b] School of Mechatronic Engineering and Automation, Shanghai University, Shanghai, PR China

ARTICLE INFO

Keywords:
Biodegradable magnesium alloys
Corrosion and fracture
Multiphase-field modelling
Incremental variational principle
In vitro experiments

ABSTRACT

Biodegradable magnesium alloys have been developed as promising biomedical materials for temporary implants. To facilitate the development of implant design, it is essential to understand and quantify the corrosion behaviour of magnesium alloys under mixed chemo-mechanical loadings. In this study, a multiphase-field model is proposed based on the variational principle to capture the interactions between corrosion and ductile fracture in biodegradable magnesium alloys. Multiple order parameters are introduced to track the interfaces associated with crack propagation and magnesium dissolution. The deformation-fracture-corrosion interactions are considered in the energetic variational formulation with coupling functions. The governing equations are discretised using an incremental variational method and solved by a staggered scheme. Parametric studies on the coupling functions are performed to demonstrate the flexibility of the model. The proposed multiphase-field model is calibrated and validated by in vitro experiments with tensile specimens of rare-earth magnesium alloy WE43MEO. The experimental and computational results demonstrate that the proposed model can capture the degradation and stress corrosion cracking behaviours in the immersion tests and slow strain rate tensile-corrosion tests.

1. Introduction

Magnesium alloys have been widely studied for their potential biomedical applications as biodegradable implant materials. Compared to their existing polymers and bioactive glasses counterparts, magnesium alloys possess higher mechanical strength and similar stiffness to that of bone for orthopaedic applications (Staiger et al., 2006; Niinomi et al., 2012). Moreover, in vitro and in vivo studies have confirmed that magnesium alloys exhibit good biocompatibility to reduce chronic inflammation and late stent thrombosis (Kamrani and Fleck, 2019). Their inherent ability to dissolve within the human body eliminates the need for a second surgery, thereby lessening the associated costs on patients and social healthcare systems (Chakraborty Banerjee et al., 2019). Despite the mentioned advantages, premature failure of biodegradable magnesium implants due to the undesirable degradation rate in the physiological environment limited extensive clinical applications (Hänzi et al., 2010; Choudhary and Raman, 2012). Therefore, the implant design should be optimised for sufficient resistance to cracking in the human body under the combined effects of corrosive body fluids and mechanical loadings (Jafari et al., 2015a).

To understand and quantify the corrosion process of magnesium alloys under physiological conditions, many research efforts have been devoted to in vitro and in vivo corrosion studies of magnesium implants. Jang et al. (2013) evaluated the effect of the

* Corresponding author.
E-mail address: ma@iam.rwth-aachen.de (S. Ma).

https://doi.org/10.1016/j.jmps.2024.105694
Received 14 October 2023; Received in revised form 12 April 2024; Accepted 22 May 2024
Available online 29 May 2024

ions in physiological plasma on the corrosion behaviour of Mg alloys. The experimental results demonstrated that in vitro corrosive environments play an important role in the synthesis of protective corrosion products, thus affecting corrosion rates of the alloy. In vitro and in vivo experiments of magnesium alloys conducted by Hofstetter et al. (2015) showed that the local electrochemical attack and the galvanically accelerated dissolution of the magnesium matrix cause the formation of pits, leading to inhomogeneous degradations of biodegradable Mg implants. Nachtsheim et al. (2022) have analysed the composition and microstructure of the corrosion products formed on the WE43 Mg alloys after long-term in vitro corrosion. By investigating the effect of mechanical loading on corrosion, Gao et al. (2019) reported that compressive stresses have minimal effects on the degradation of high-purity magnesium implants, while tensile stresses significantly accelerate the in vitro corrosion process. Moreover, in vitro studies conducted by Dubey et al. (2019) have shown that the mechanical integrity of degradable magnesium alloys primarily decreases as a result of pitting corrosion, and the growth of corrosion pits and cracks mutually accelerate each other.

The corrosive physiological environment and dynamic mechanical loadings during daily physical activities induce a risk of stress corrosion cracking (SCC) in biodegradable Mg implants, potentially leading to crack formation and failure of implants. SCC in Mg alloys is usually attributed to two primary mechanisms: (1) continuous crack propagation driven by anodic dissolution at the crack tip, where mechanical stresses result in a local rupture of the passive film between the alloy matrix and electrolyte near the crack tip; (2) hydrogen embrittlement, where atomic hydrogen generated during the electrochemical corrosion process can penetrate the Mg alloy matrix and attenuate its mechanical strength (Winzer et al., 2005). Depending on materials and corrosion environments, either one of the two mechanisms can be dominant, or both mechanisms can be observed concurrently. In the anodic dissolution-dominated case (*e.g.* AZ31B in $NaCl+K_2CrO_4$ solution (Logan, 1958)), the specimen exhibits prominent pitting characteristics with rapid local localised dissolution. On the other hand, in the environmental-assisted fracture-dominated case (*e.g.* AZ91D in simulated body fluids) (Choudhary and Raman, 2013)), the final failure form of the specimen is more inclined towards fracture. In particular, Jafari et al. (2015b), Choudhary et al. (2014) characterised the SCC behaviour of WE43 alloy in simulated body fluids as a mixed-mode mechanism in in vitro experiments. A better insight into SCC in biodegradable Mg alloys is indispensable for facilitating the design and optimisation of Mg implants.

To this end, various computational models have been proposed in the last decades to predict corrosion and fracture in biodegradable Mg alloys, including phenomenological and physical models. The continuum damage mechanics (CDM)-based phenomenological model provides a framework to describe the damage process by incorporating damage parameters for distinct damage mechanisms (Ma and Yuan, 2015; Ma et al., 2016). These damage parameters capture the evolution of corrosion damage and material degradation, enabling a comprehensive representation of the SCC behaviour of biodegradable Mg alloys. Gastaldi et al. (2011) developed a CDM model to simulate the degradation process of bioabsorbable Mg stents by combining uniform corrosion and stress corrosion damages. Grogan et al. (2011) extended the CDM model of the uniform corrosion to predict the pitting corrosion behaviour by introducing stochastic variations of corrosion properties. This model was recently employed by van Gaalen et al. (2023a) to predict the mechanical integrity degradation of bioabsorbable magnesium alloy WE43MEO under various corrosion scenarios. Ma et al. (2018) proposed an integrative computational framework for modelling the degradation process of Mg implants under physiological loadings to account for tissue differentiation of fractured bones during bone healing. Although the CDM model has been extended to incorporate the transport of Mg species (Grogan et al., 2014), it still lacks a comprehensive physical explanation for the electrochemical phenomena of SCC. Recently, peridynamics (PD) was utilised by De Meo et al. (2016) for modelling of the hydrogen-assisted corrosion cracking based on the adsorption-induced decohesion mechanism. Chen et al. (2021) proposed a fully coupled fracture-corrosion PD model to capture the pit-to-crack transition phenomena by neglecting the diffusion of species. Hermann et al. (2022) predicted the residual strength of degradable Mg implants by integrating the PD corrosion model in the finite element method framework. However, the applications of these nonlocal PD models are stilled limited owing to the high computational complexity and difficulties in the treatment of boundary conditions (Jafarzadeh et al., 2019).

The DMEM or other cell culture media have very complex chemical compositions, including multiple ions and organic components (Rohanová et al., 2014), which lead to very complicated mechano-electrochemical processes of formation/rupture/dissolution of corrosion products and play an important role in the underlying corrosion mechanisms. In addition, the chemical compositions of magnesium alloys significantly affect the formation/dissolution of corrosion products (Esmaily et al., 2017). The ions and organic components continuously react with the corrosion products in the long-term corrosion process, resulting in spatial and temporal evolutions of the corrosion layer. For instance, the presence of HPO_4^{2-} and HCO_3^- in physiological environments can transform $Mg(OH)_2$ into insoluble tertiary magnesium phosphate, $Mg_3(PO_4)_2$ (Xin et al., 2008), and more stable giorgiosite, $Mg_5(CO_3)_4(OH)_4 5H_2O$ (Lindström et al., 2004), respectively. Moreover, the adsorption of protein to the specimen can form another protective layer to block the anodic reaction (Liu et al., 2007). Recently, computational studies attempted to elaborate physics-based models for modelling the formation/dissolution of corrosion products in the degradation process of magnesium alloys (Sanz-Herrera et al., 2018; Barzegari et al., 2021; Sun et al., 2013; Höche, 2014). However, most models did not account for the effects of complex multiple ions and organic components of simulated body fluids, leading to a high inaccuracy of simulation results. Therefore, a number of phenomenological material parameters were additionally introduced to fit the experimental results. Especially, Zeller-Plumhoff et al. (2022) considered the realistic compositions of in vitro corrosion medium in the corrosion simulation of magnesium alloys. Nevertheless, the simulations focused on the microscale corrosion and required very high computation costs for the macroscale prediction.

As a promising and versatile method, phase-field (PF) models have been recently developed for modelling environment-assisted crack propagation and stress-assisted corrosion. In the phase-field theory, the sharp interface between two different material states is smeared by a diffusive interface, and its movement is implicitly tracked by the evolution of phase field variable, thus avoiding the computational problem caused by moving boundaries (Zhou et al., 2019). The fracture PF models based on the

variational framework developed by Francfort and Marigo (1998) and Bourdin et al. (2000) have been extended to account for the environmental effects, including the hydrogen embrittlement (Duda et al., 2018; Martínez-Pañeda et al., 2018; Kristensen et al., 2020; Isfandbod and Martínez-Pañeda, 2021) and metallic ion diffusion (Ahmadi, 2020; Zhang et al., 2016). In the context of stress-assisted corrosion, several phase-field models have been proposed for considering coupling effects among deformation, fracture and corrosion. The models developed by Ståhle and Hansen (2015) and Nguyen et al. (2018) coupled the corrosion field to strain energy, which contributes to the corrosion driving force. Mai and Soghrati (2017) and Cui et al. (2021, 2022) coupled the interface kinetics parameter of the Allen-Cahn equation to mechanical deformations based on the film-rupture-model and Gutman's model, respectively. Meanwhile, the multifield model proposed in Cui et al. (2022) embedded hydrogen embrittlement in the constitutive description of the corrosion and deformation behaviours. Lin and Ruan (2021) formulated a mechanochemical PF model for considering electrochemical interactions between different ions. More recently, PF models have been employed to study the degradation and stress-corrosion processes of bioabsorbable Mg alloys under external loads (Kovacevic et al., 2023; Xie et al., 2022). However, most PF models for magnesium alloys typically neglect the protective effect of corrosion products on the alloy surface. This implies that the electrolyte is assumed to directly interact with the exposed alloy matrix, which cannot accurately represent the corrosion behaviour of magnesium alloys in vitro and in vivo. Furthermore, among the currently developed corrosion models, the evolution of fracture and corrosion interfaces is tracked by a single order parameter (Chen et al., 2021; Cui et al., 2021), which cannot accurately capture their interactions in the SCC process of biodegradable Mg alloys (Gutman, 2007).

The objective of this work is to develop a phenomenological model based on the multiphase field method for predicting the corrosion-fracture behaviour of magnesium alloys under mechanochemical loadings at macroscopic space/time scales and validate the simulation results by macroscopic in vitro experiments. In this work, we develop a variational-based framework for the multiphase-field modelling of degradation and stress corrosion cracking in biodegradable Mg alloys. The model incorporates two main mechanisms: (i) corrosion increases the material's susceptibility to fracture, and (ii) micro and macrocracks in passive film and corrosion products enhance the electrolyte's permeability. Parametric studies of three physically significant coupling functions showcase the current model's versatility in modelling degradation behaviour of magnesium alloys. Furthermore, the model is calibrated and validated by in vitro corrosion experiments, tensile tests and stress corrosion tests of specimens manufactured from biomedical magnesium alloy WE43MEO, already being in clinical use for bioabsorbable orthopaedic implants. The reasonable agreement between experimental results and computational predictions demonstrates the predictive capacity of the model in characterising the corrosion-fracture behaviours of biodegradable Mg alloys. The paper is organised as follows. In Sections 2 and 3, we present the rate-type variational formulations of the phase-field model and its numerical discretisation approach based on the incremental finite element method. The material and experimental methodology are given in Section 4. In Section 5, model parameters are calibrated according to the experimental results, and parametric studies are conducted to quantitatively analyse the effects of model parameters in the coupling functions. Conclusions and remarks are summarised in Section 6.

2. A variational framework of ductile fracture coupled with corrosion

In this section, we summarise the developed multiphase-field model for describing the coupled degradation and fracture in a variational framework. A proper construction of a mixed variational framework allows us to model the coupled evolutionary system based on the stationarity of a rate-type potential functional.

2.1. Problem outline

When Mg alloys are exposed to an aqueous environment, chemical reactions occurring on the surface of Mg alloys lead to the formation of a passive layer consisting of various corrosion products. This growing layer hinders water access to the alloy matrix and impedes the transport of ions, ultimately resulting in a reduced corrosion rate (Hornberger et al., 2012; Ascencio et al., 2014). The corrosion layer in in vitro and in vivo conditions, consisting of an inner layer of MgO and an outer thick layer of Mg-O-Ca-P (Santamaria et al., 2007), protects the Mg alloy matrix from corrosion. However, due to its easily cleavable features, the corrosion layer is susceptible to damage under mechanochemical loadings. If the corrosion layer is too thin or completely cracked in certain regions, corrosion will occur with a higher rate in those areas, leading to the formation of pits. The corrosion process can be modelled by being divided into two processes, the chemical reaction occurring at the corrosion interface and ion diffusion in the electrolyte. When the rate of electrochemical reaction is limited by the rate of diffusion of ions, this process is referred to as diffusion-controlled corrosion. In contrast, if the reaction rate is very slow, the process is activation-controlled. In this study, we focus on the long-term stress-assisted degradation behaviour of Mg alloys and therefore ignore the explicit chemical kinetics of complex ion compositions of the electrolyte in the corrosion process. Moreover, it is assumed that the coupling between material cracking and the diffusion-controlled corrosion are mainly attributed to the mechanisms: (i) corrosion diminishes the fracture toughness of the material, (ii) cracking in the alloy matrix and corrosion products enhances the diffusivity of species.

2.2. Global primary fields

As illustrated in Fig. 1, we consider a mixing domain of magnesium alloy and electrolyte (corrosion environment) $\Omega \subset \mathbb{R}^3$ with external boundary $\partial\Omega$, which is decomposed into a solid boundary $\partial\Omega_s$ and an electrolyte boundary $\partial\Omega_l$ with $\partial\Omega = \partial\Omega_s + \partial\Omega_l$ and $\partial\Omega_s \cap \partial\Omega_l = \varnothing$. It is supposed that the electrolyte does not flow but only conducts ions by diffusion. The displacement of the domain is defined by the displacement field $\boldsymbol{u}(\boldsymbol{x}, t)$ with $\boldsymbol{u} = \bar{\boldsymbol{u}}(\boldsymbol{x})$ on the displacement boundary $\partial\Omega_{\boldsymbol{u}}^{u}$ and a surface traction $\boldsymbol{t} = \bar{\boldsymbol{t}}(\boldsymbol{x})$ on

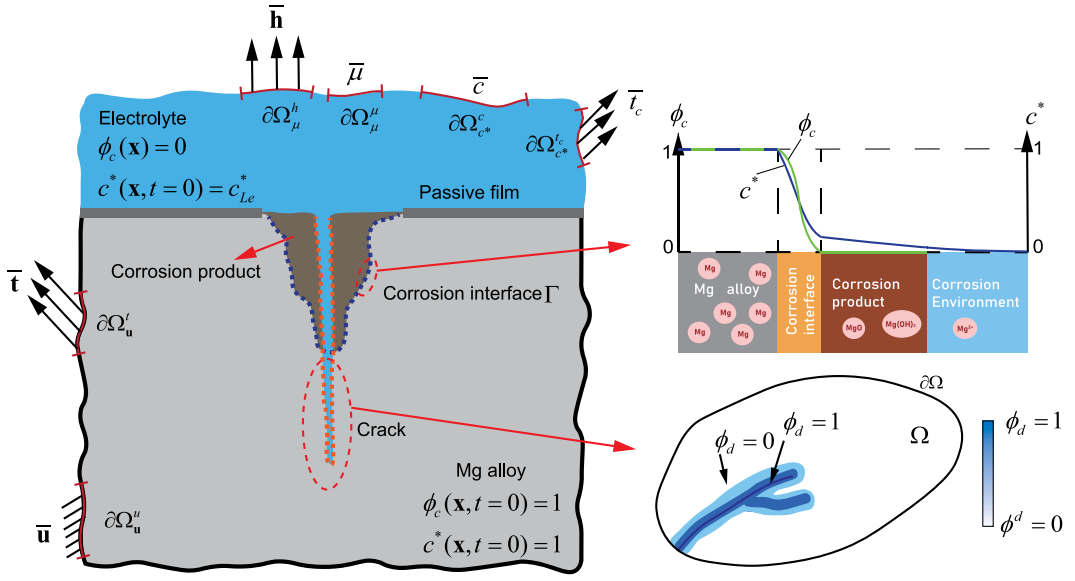

Fig. 1. Schematic of the multiphase-field framework proposed for modelling material dissolution and fracture of biodegradable magnesium alloys. The model includes two auxiliary phase field variables for the corrosion (ϕ_c) and cracking (ϕ_d) processes. Both corrosion products and electrolytes have the value of the corrosion field $\phi_c = 0$. The distinction between corrosion products and electrolytes is achieved with the help of the crack field. The rupture of corrosion products ($\phi_d = 1$, $\phi_c = 0$) denotes the transition of the region into electrolyte.

the traction boundary $\partial\Omega^t_{\boldsymbol{u}}$. The Mg concentration field of the domain is defined by introducing the normalised ion concentration $c^*(\boldsymbol{x},t) = c(\boldsymbol{x},t)/c_{\text{solid}}$, where c_{solid} is the equilibrium concentration of Mg in the solid, with $c^* = \bar{c}(\boldsymbol{x})$ on the concentration boundary $\partial\Omega^c_{c^*}$ and a microscopic traction $\bar{\boldsymbol{t}}_c(\boldsymbol{x})$ on the boundary $\partial\Omega^{t_c}_{c^*}$ prescribed by Neumann-type conditions. The flux of the Mg ions is driven by the chemical potential μ, with $\mu = \bar{\mu}$ on the potential boundary $\partial\Omega^{\mu}_{\mu}$ and flux boundary condition $\boldsymbol{h} = \bar{\boldsymbol{h}}$ on the $\partial\Omega^h_{\mu}$. The mentioned six boundaries are restricted to

$$\begin{aligned}&\partial\Omega = \partial\Omega^u_{\boldsymbol{u}} + \partial\Omega^t_{\boldsymbol{u}} \quad \text{with} \quad \partial\Omega^u_{\boldsymbol{u}} \cap \partial\Omega^t_{\boldsymbol{u}} = \emptyset, \quad \partial\Omega = \partial\Omega^c_{c^*} + \partial\Omega^{t_c}_{c^*} \quad \text{with} \quad \partial\Omega^c_{c^*} \cap \partial\Omega^{t_c}_{c^*} = \emptyset,\\ &\text{and} \quad \partial\Omega = \partial\Omega^{\mu}_{\mu} + \partial\Omega^h_{\mu} \quad \text{with} \quad \partial\Omega^{\mu}_{\mu} \cap \partial\Omega^h_{\mu} = \emptyset.\end{aligned} \tag{1}$$

In the present multiphase-field model, two auxiliary phase variables ϕ_d and ϕ_c are introduced. ϕ_d tracks the crack interface in solids with $\phi_d = 0$ for intact material points and $\phi_d = 1$ for completely fractured state. Furthermore, ϕ_d is a passive state field without corresponding external loading as $\nabla\phi_d \cdot \boldsymbol{n} = 0$ on $\partial\Omega$. By defining $\phi_c = 0$ for the totally corroded material and $\phi_c = 1$ for the uncorroded alloy matrix, ϕ_c varies continuously across the corrosion interface Γ_c. When the material undergoes complete corrosion $\phi_c = 0$, a fragile layer of intact corrosion products adheres to the alloy's surface. Under external loading, these corrosion products fracture and facilitate the influx of electrolyte. Consequently, the specific condition with $\phi_c = 0$ and $\phi_d = 1$ denotes the transition of the region into electrolyte. Considering ϕ_c being always 0 in the corrosion environment and no corresponding external tractions on the solid boundary, the boundary conditions for the corrosion phase-field are $\phi_c = 0$ on $\partial\Omega_l$ and $\nabla\phi_c \cdot \boldsymbol{n} = 0$ on $\partial\Omega_s$. Globally, the state of the domain is characterised by displacement $\boldsymbol{u}(\boldsymbol{x},t)$, Mg concentration $c^*(\boldsymbol{x},t)$, chemical potential $\mu(\boldsymbol{x},t)$, crack phase-field variable $\phi_d(\boldsymbol{x},t)$ and corrosion phase-field variable $\phi_c(\boldsymbol{x},t)$. The primary multifield setting of state variables for the coupled chemo-mechanical problem is thus defined as

$$\mathbf{c} := \{\boldsymbol{u}, c^*, \mu, \phi_d, \phi_c\}, \tag{2}$$

where

$$\boldsymbol{u} : \Omega\times\mathcal{T} \to \mathbb{R}^3, \quad c^* : \Omega\times\mathcal{T} \to \mathbb{R}^1, \quad \mu : \Omega\times\mathcal{T} \to \mathbb{R}^1, \quad \phi_d : \Omega\times\mathcal{T} \to \mathbb{R}^1, \quad \phi_c : \Omega\times\mathcal{T} \to \mathbb{R}^1, \tag{3}$$

and the boundary conditions are prescribed as

$$\begin{aligned}&\bar{\boldsymbol{u}} : \partial\Omega^u_{\boldsymbol{u}}\times\mathcal{T} \to \mathbb{R}^3, \quad \bar{\boldsymbol{t}} : \partial\Omega^t_{\boldsymbol{u}}\times\mathcal{T} \to \mathbb{R}^3, \quad \bar{c} : \partial\Omega^c_{c^*}\times\mathcal{T} \to \mathbb{R}^1, \quad \bar{\boldsymbol{t}}_c : \partial\Omega^{t_c}_{c^*}\times\mathcal{T} \to \mathbb{R}^3,\\ &\bar{\mu} : \partial\Omega^{\mu}_{\mu}\times\mathcal{T} \to \mathbb{R}^1, \quad \bar{\boldsymbol{h}} : \partial\Omega^h_{\mu}\times\mathcal{T} \to \mathbb{R}^3.\end{aligned} \tag{4}$$

2.3. Rate-type potential functional

To describe the complex evolutions of the aforementioned primary fields $\mathbf{c}$ during the degradation and stress corrosion cracking in biodegradable Mg alloys, we construct a mixed variational framework based on a rate-type potential functional. The evolution

equations are governed by the stationarity of the rate-type potential functional Π, which is defined for the multifield problem as

$$\Pi(\dot{\boldsymbol{u}}, \dot{\phi}_d, \dot{c}^*, \mu, \dot{\phi}_c, \dot{\mathfrak{q}}, \dot{\mathfrak{f}}, \boldsymbol{h}) = \frac{d}{dt}\Psi(\boldsymbol{u}, \phi_d, c^*, \phi_c, \mathfrak{q}) + \mathfrak{D}(\dot{\phi}_d, \dot{\phi}_c, \mu, \dot{\mathfrak{q}}, \dot{\mathfrak{f}}) - P(\dot{\boldsymbol{u}}, \dot{c}^*, \boldsymbol{h}) \tag{5}$$

at a given state $\{\boldsymbol{u}, \phi_d, c^*, \phi_c, \mu, \mathfrak{q}\}$. Here, the set of local constitutive variables $\mathfrak{q}$ is introduced, and $\mathfrak{f}$ contains the local dissipative forces and associated Lagrange multipliers. The free energy functional Ψ takes the form

$$\Psi(\boldsymbol{u}, \phi_d, c^*, \phi_c, \mathfrak{q}) = \int_\Omega \psi(\nabla_s \boldsymbol{u}, \phi_d, c^*, \phi_c, \nabla c^*, \mathfrak{q})\, dV, \tag{6}$$

where ψ is the local free energy density. The system dissipation incorporates the dissipation mechanisms due to plastic deformation, fracture, diffusion and corrosion processes, resulting in a general form of dissipation potential functional $\mathfrak{D}$

$$\mathfrak{D}(\dot{\phi}_d, \dot{\phi}_c, \mu, \dot{\mathfrak{q}}, \dot{\mathfrak{f}}) = \int_\Omega \upsilon^*(\dot{\phi}_d, \dot{\phi}_c, \boldsymbol{h}, \mathbb{M}, \dot{\mathfrak{q}}, \dot{\mathfrak{f}})\, dV \tag{7}$$

with υ^* being the local dissipation potential density. The local ion out-flux $\boldsymbol{h}$ is defined by $\boldsymbol{h} := \partial_{\mathbb{M}} \upsilon^*$. $\mathbb{M}$ is the spatial derivative of μ and defined as

$$\mathbb{M} = -\nabla \mu(\boldsymbol{x}, t). \tag{8}$$

The external power functional consists of a chemomechanical contribution P^m and a diffusive contribution P^h following

$$P(\dot{\boldsymbol{u}}, \dot{c}^*, \boldsymbol{h}) = P^m(\dot{\boldsymbol{u}}, \dot{c}^*) + P^h(\boldsymbol{h}). \tag{9}$$

The chemomechanical contribution produced by the macro and the micro surface tractions is given as

$$P^m(\dot{\boldsymbol{u}}, \dot{c}^*) = \int_\Omega \mathbf{b} \cdot \dot{\mathbf{u}}\, dV + \int_{\partial\Omega^t_{\boldsymbol{u}}} \bar{\boldsymbol{t}} \cdot \dot{\mathbf{u}}\, dA + \int_{\partial\Omega^{t_c}_{c^*}} \bar{\boldsymbol{t}}_c \cdot \boldsymbol{n} \dot{c}^*\, dA, \tag{10}$$

involving the body force $\boldsymbol{b}$ per unit volume, the macro and micro surface traction $\bar{\boldsymbol{t}}$ and $\bar{\boldsymbol{t}}_c$. The external flux contribution due to specie transports takes the form

$$P^h(\boldsymbol{h}) = \int_{\partial\Omega^\mu_\mu} -\bar{\mu} \boldsymbol{h} \cdot \boldsymbol{n}\, dA, \tag{11}$$

where $\bar{\mu}$ is the prescribed chemical potential on the boundary $\partial\Omega^\mu_\mu$. It is worth emphasising that the out-flux $\boldsymbol{h}$ in this context refers to the transport of the magnesium ions after ionisation.

2.3.1. Specification of free energy functional

The stored energy functional is decomposed into the elasto-plastic free energy and the chemical free energy

$$\Psi = \Psi^{ep} + \Psi^{ch} = \int_\Omega \left[\psi^{ep}(\boldsymbol{\varepsilon}, \boldsymbol{\varepsilon}^p, \gamma, \phi_d) + \psi^{ch}(\phi_c, c^*, \nabla c^*)\right] dV. \tag{12}$$

The elasto-plastic free energy density ψ^{ep} depends on the macroscopic strain $\boldsymbol{\varepsilon}$, the plastic strain $\boldsymbol{\varepsilon}^p$, the internal variable γ and the fracture phase-field ϕ_d. Considering the small-strain theory, the strain tensor can be defined as the symmetric part of the spatial gradient of the displacement field:

$$\boldsymbol{\varepsilon} = \nabla_s \boldsymbol{u} = \frac{1}{2}\left(\nabla \boldsymbol{u} + \nabla^T \boldsymbol{u}\right). \tag{13}$$

$\boldsymbol{\varepsilon}$ is decomposed into its elastic $\boldsymbol{\varepsilon}^e$ and plastic $\boldsymbol{\varepsilon}^p$ parts with $\boldsymbol{\varepsilon} = \boldsymbol{\varepsilon}^e + \boldsymbol{\varepsilon}^p$. Furthermore, the description of the isotropic hardening phenomenon requires an additional scalar isotropic hardening variable γ. To prevent the interpenetration of the crack region under compression, the volumetric/deviatoric split method proposed by Amor et al. (2009) is utilised in the formulation of the elastic free energy density. In this context, the strain tensor is decomposed into its spherical and deviatoric parts

$$\boldsymbol{\varepsilon} = \boldsymbol{\varepsilon}_S + \boldsymbol{\varepsilon}_D, \quad \boldsymbol{\varepsilon}_S = \frac{1}{3}\mathrm{tr}(\boldsymbol{\varepsilon})\boldsymbol{I}, \quad \boldsymbol{\varepsilon}_D = \boldsymbol{\varepsilon} - \frac{1}{3}\mathrm{tr}(\boldsymbol{\varepsilon})\boldsymbol{I}, \tag{14}$$

where $\boldsymbol{I}$ is the second-order identity tensor. By introducing the elastic deviatoric strain $\boldsymbol{\varepsilon}^e_D = \boldsymbol{\varepsilon}_D - \boldsymbol{\varepsilon}^p_D$, where $\boldsymbol{\varepsilon}^p_D := \boldsymbol{\varepsilon}^p - \frac{1}{3}\mathrm{tr}(\boldsymbol{\varepsilon}^p)\boldsymbol{I}$ is the deviatoric part of plastic strain, the elastic–plastic free energy density is defined as a combination of the elastic free energy density ψ^{el} and the free energy density ψ^{hard} due to the isotropic hardening as:

$$\psi^{ep} = \psi^{el}(\boldsymbol{\varepsilon}, \boldsymbol{\varepsilon}^p, \phi_d) + \psi^{hard}(\gamma, \phi_d), \tag{15}$$

with

$$\psi^{el}(\boldsymbol{\varepsilon}, \boldsymbol{\varepsilon}^p, \phi_d) = h_d(\phi_d)\left[\frac{1}{2}\bar{K}\langle \mathrm{tr}(\boldsymbol{\varepsilon} - \boldsymbol{\varepsilon}^p)\rangle^2 + \bar{G}\left(\boldsymbol{\varepsilon}_D - \boldsymbol{\varepsilon}^p_D\right) : \left(\boldsymbol{\varepsilon}_D - \boldsymbol{\varepsilon}^p_D\right)\right] + \frac{1}{2}\bar{K}\langle -\mathrm{tr}(\boldsymbol{\varepsilon} - \boldsymbol{\varepsilon}^p)\rangle^2, \tag{16}$$

$$\psi^{hard}(\gamma, \phi_d) = \frac{1}{2}h_d(\phi_d)\bar{H}\gamma^2, \tag{17}$$

where $\bar{K} > 0$ and $\bar{G} > 0$ are effective (undamaged) bulk and shear modulus respectively. The degradation function, $h_d(\phi_d) = (1-\phi_d)^2$, captures the degradation of the mechanical properties of material due to damage. For simplification, we ignore the effect of corrosion

on mechanical deformations, since the deformation behaviour of corrosion products of biodegradable magnesium alloys are not available in literature. The McAuley brackets $\langle\cdot\rangle$ are defined as $\langle x\rangle = \max(x, 0)$. $\bar{H}$ is the effective hardening modulus. Eq. (16) implies that only the strain energy induced by tension and shear drives the damage and crack propagation in the material.

The chemical free energy density ψ^{ch} is expressed as a function of the corrosion phase-field ϕ_c and the normalised ion concentration c^*, which incorporates the bulk part ψ^{ch}_{bulk} and the interfacial part ψ^{ch}_{grad}

$$\psi^{ch}(c^*, \phi_c, \nabla c^*) = \psi^{ch}_{bulk}(c^*, \phi_c) + \psi^{ch}_{grad}(\nabla c^*), \tag{18}$$

where the interfacial energy density is given

$$\psi^{ch}_{grad} = \kappa \nabla c^* \cdot \nabla c^*. \tag{19}$$

Here, κ is the concentration gradient energy coefficient (Cahn and Hilliard, 1958). The chemical bulk free energy is constructed as

$$\psi^{ch}_{bulk}(c^*, \phi_c) = A\left[c^* - \left(1 - h_c(\phi_c)\right) c^*_{Le} - h_c(\phi_c) c^*_{Se}\right]^2, \tag{20}$$

with details given in Appendix A. Here, A is the free energy density curvature and $h_c(\phi_c)$ is a continuous interpolation function such that $h_c(\phi_c = 0) = 0$ and $h_c(\phi_c = 1) = 1$. In this study, a cubic function $h_c(\phi_c) = -2{\phi_c}^3 + 3{\phi_c}^2$ is used following (Mai et al., 2016). $c^*_{Se} = 1$ and c^*_{Le} are the normalised equilibrium concentration in the metal matrix and corroded material, respectively.

2.3.2. Rate of free energy functional

Taking the time derivative of Eq. (12), one obtains the rate of the energy stored at a given state $\{\boldsymbol{\varepsilon}, \boldsymbol{\varepsilon}^p, \gamma, \phi_d, \phi_c, c^*, \nabla c^*\}$

$$\dot{\Psi} = \int_\Omega \left(\boldsymbol{\sigma} : \dot{\boldsymbol{\varepsilon}} - \boldsymbol{\sigma} : \dot{\boldsymbol{\varepsilon}}^p + \sigma_\gamma \dot{\gamma} + \sigma_f \dot{\phi}_d + \sigma_{\phi_c} \dot{\phi}_c + \sigma_c \dot{c}^*\right) dV + \int_{\partial\Omega} \kappa \nabla c^* \cdot \boldsymbol{n} \dot{c}^* \, dA, \tag{21}$$

where $\boldsymbol{\sigma}$ is the stress tensor and derived as

$$\boldsymbol{\sigma} := \partial_{\boldsymbol{\varepsilon}} \psi^{el} = h_d \left[\bar{K}\langle \mathrm{tr}(\boldsymbol{\varepsilon} - \boldsymbol{\varepsilon}^p)\rangle \boldsymbol{I} + 2\bar{G}\boldsymbol{\varepsilon}^e_D\right] - \bar{K}\langle -\mathrm{tr}(\boldsymbol{\varepsilon} - \boldsymbol{\varepsilon}^p)\rangle \boldsymbol{I}. \tag{22}$$

σ_γ, σ_f, σ_{ϕ_c} and σ_c are the generalised energetic forces conjugate to γ, ϕ_d, ϕ_c and c^* respectively, and defined by

$$\begin{aligned} \sigma_\gamma &:= \partial_\gamma \psi^{hard} = \bar{H} h_d(\phi_d)\gamma, & \sigma_f &:= \partial_{\phi_d} \psi^{ep} = h'_d(\phi_d)\bar{\psi}^{ep+}, \\ \sigma_{\phi_c} &:= \partial_{\phi_c} \psi^{ch}, & \sigma_c &:= \partial_{c^*} \psi^{ch} - \nabla \cdot \partial_{\nabla c^*} \psi^{ch}, \end{aligned} \tag{23}$$

where $\bar{\psi}^{ep+} := \frac{1}{2}\bar{K}\langle \mathrm{tr}(\boldsymbol{\varepsilon} - \boldsymbol{\varepsilon}^p)\rangle^2 + \bar{G}\boldsymbol{\varepsilon}^e_D : \boldsymbol{\varepsilon}^e_D + \frac{1}{2}\bar{H}\gamma^2$ is the effective positive elasto-plastic free energy, and $h'_d(\phi_d)$ denotes the derivative of the degradation function $h_d(\phi_d)$ with respect to ϕ_d.

2.3.3. Specification of dissipation potential functional

The dissipation during degradation and fracture processes in biodegradable magnesium alloys is attributed to plastic deformation, fracture, chemical reaction and diffusion. Accordingly, the rate of the dissipation potential functional is decomposed into:

$$\mathfrak{D} = \mathfrak{D}^p + \mathfrak{D}^d + \mathfrak{D}^{ch} + \mathfrak{D}^{pd} + \mathfrak{D}^{dc}, \tag{24}$$

where $\mathfrak{D}^p$, $\mathfrak{D}^d$ and $\mathfrak{D}^{ch}$ denote the plastic dissipation potential, the fracture dissipation potential and the chemical corrosion dissipation potential, respectively. Two additional terms $\mathfrak{D}^{pd}$ and $\mathfrak{D}^{dc}$ are introduced to enable the strong coupling between plastic deformation and fracture, fracture and corrosion, respectively.

To specify the plastic dissipation density, the dissipative forces $\boldsymbol{s}_p$ and β are introduced dual to $\dot{\boldsymbol{\varepsilon}}^p$ and $\dot{\gamma}$, respectively. By assuming isotropic plastic deformation behaviours of magnesium alloys, the yield function is defined according to the J_2 plasticity theory as

$$f_p(\boldsymbol{s}_p, \beta; \boldsymbol{\varepsilon}^p, \gamma, \phi_d) := \sqrt{\frac{3}{2}}\|\mathrm{dev}[\boldsymbol{s}_p]\| - \beta - \sigma_y \le 0, \tag{25}$$

where $\mathrm{dev}[\boldsymbol{s}_p]$ is the deviatoric part of the tensor $\boldsymbol{s}_p$. σ_y is the degraded initial yield stress and computed by the degradation function $h_d(\phi_d)$ and the undamaged initial yield stress $\bar{\sigma}_y$

$$\sigma_y = h_d(\phi_d)\bar{\sigma}_y. \tag{26}$$

The extended plastic dissipation functional including the yield function for the constrained problem is then expressed as

$$\mathfrak{D}^p(\boldsymbol{s}_p, \dot{\boldsymbol{\varepsilon}}^p, \beta, \dot{\gamma}, \lambda_p) = \int_\Omega \left[\boldsymbol{s}_p : \dot{\boldsymbol{\varepsilon}}^p - \beta\dot{\gamma} - \lambda_p\left(\sqrt{\frac{3}{2}}\|\mathrm{dev}[\boldsymbol{s}_p]\| - \beta - \sigma_y\right)\right] dV, \tag{27}$$

where λ_p is the Lagrange multiplier field associated with the constraint $f_p \le 0$.

Following the variational principle proposed in Miehe et al. (2010), the rate-type fracture dissipation potential functional at a given state $\{\phi_d, \phi_c\}$ is formulated based on thermodynamic consistency conditions, incorporating the irreversibility of fracture

$$\mathfrak{D}^d(\xi, \dot{\phi}_d, \lambda_d) = \int_\Omega \left[\xi\dot{\phi}_d - \lambda_d f_d(\xi, \phi_d)\right] dV, \tag{28}$$

where ξ is the dissipative force dual to the crack phase-field $\dot{\phi}_d$ and λ_d is the Lagrange multiplier field associated with the constraint f_d. Regarding a discontinuous and rate-independent crack evolution process, the local threshold function f_d is introduced as

$$f_d(\xi, \phi_d) = \xi - r_f \leq 0 \quad \text{with} \quad r_f := g_d \delta_{\phi_d} \gamma_d(\phi_d, \nabla\phi_d), \tag{29}$$

where r_f is the fracture dissipative resistance. g_d is the fracture energy required to form a unit area of crack and considered to decrease during the corrosion process as a function of the corrosion phase-field ϕ_c, that is

$$g_d(\phi_c) = h_{dc}(\phi_c) g_{dm} + [1 - h_{dc}(\phi_c)] g_{dc}, \tag{30}$$

where g_{dm} and g_{dc} are the fracture energy of uncorroded material and totally corroded material, respectively. The degradation function h_{dc} is constructed following

$$h_{dc}(\phi_c = 0) = 0, \; h_{dc}(\phi_c = 1) = 1, \; h'_{dc}(\phi_c = 0) = 0 \text{ and } h'_{dc}(\phi_c = 1) = 0. \tag{31}$$

Here we take the form

$$h_{dc}(\phi_c) = -m_c \phi_c^{m_c+1} + (m_c + 1)\phi_c^{m_c}, \tag{32}$$

where $m_c \geq 2$ is a model parameter. The cubic function ($m_c = 2$) is introduced by Kuhn et al. (2015) and the quartic function ($m_c = 3$) is adopted by Karma et al. in Karma et al. (2001). $\delta_{\phi_d} \gamma_d(\phi_d, \nabla\phi_d)$ is the variational derivative of the fracture surface density function $\gamma_d(\phi_d, \nabla\phi_d)$ and defined as

$$\delta_{\phi_d} \gamma_d(\phi_d, \nabla\phi_d) := \partial_{\phi_d} \gamma_d - \nabla \cdot \partial_{\nabla\phi_d} \gamma_d, \quad \text{with} \quad \gamma_d(\phi_d, \nabla\phi_d) = \frac{l_d}{2} \nabla\phi_d \cdot \nabla\phi_d + \frac{{\phi_d}^2}{2 l_d}, \tag{33}$$

where l_d is the fracture interface thickness adopted in the phase-field framework to regularise the sharp crack surface topology to a diffusive crack surface.

The corrosion dissipation of magnesium alloys occurs in conjunction with the species transport and chemical reactions. The dissipation potential functional of the diffusion process and phase transition process is thus specified as

$$\mathfrak{D}^{ch}(\boldsymbol{h}, \mathbb{M}, \chi, \dot{\phi}_c) = \int_\Omega \left[\boldsymbol{h} \cdot \mathbb{M} - \chi \dot{\phi}_c - v_c^*(\mathbb{M}, \chi) \right] dV, \tag{34}$$

where χ is the dissipative force dual to the corrosion phase-field and $v_c^*(\mathbb{M}, \chi)$ is the dual dissipation potential of chemical-reaction–diffusion process, defined by

$$v_c^*(\mathbb{M}, \chi) = \frac{1}{2} M_c \mathbb{M} \cdot \mathbb{M} + \frac{L_c}{2} \left(r_c - \chi \right)^2. \tag{35}$$

Here, L_c is the interface kinetics parameter of corrosion, and M_c is the diffusion mobility of specie transport. Specially, we adopt the assumption that diffusion mobility is a function of the crack phase-field ϕ_d. A crack filled with electrolyte creates a path for a rapid diffusion of ions, and therefore, it is expected that the diffusion mobility within a crack is much higher than that in intact regions. To this end, a linear function is employed to interpolate the change of the diffusion mobility between cracked and intact regions following Wu and De Lorenzis (2016).

$$M_c(\phi_d) = (1 - h_f(\phi_d)) M_{cp} + h_f(\phi_d) M_{cl}, \quad \text{and} \quad h_f(\phi_d) = \phi_d^{m_d}, \tag{36}$$

where m_d denotes a model parameter controlling the rate of diffusivity change. M_{cp} and M_{cl} are the diffusion mobilities of species in the intact corrosion products and the electrolyte, respectively, which are related with their diffusion coefficient as $M_{cp} = \frac{D_{cp}}{2A}$ and $M_{cl} = \frac{D_{cl}}{2A}$. r_c is the corrosion energy, representing the energy to be dissipated on the corrosion interface and defined by

$$r_c := \alpha_c \nabla \cdot \nabla\phi_c - w_c \partial_{\phi_c} g_w(\phi_c), \tag{37}$$

where α_c is the gradient energy coefficient associated with the corrosion phase-field. $g_w(\phi_c) = {\phi_c}^2 (1 - \phi_c)^2$ is the chemical double well potential, and w_c is the height of the imposed double-well energy barrier. It is emphasised that the conservation law of species should be satisfied for an arbitrary domain with the specified volume Ω^* and surface $\partial\Omega^*$:

$$\int_{\Omega^*} \dot{c}^* \, dV = - \int_{\partial\Omega^*} \boldsymbol{h} \cdot \boldsymbol{n} \, dA. \tag{38}$$

By applying the divergence theorem, the local form can be written as

$$\dot{c}^* = -\nabla \cdot \boldsymbol{h}. \tag{39}$$

We remind that

$$\int_\Omega \boldsymbol{h} \cdot \mathbb{M} d\Omega = \int_\Omega -\boldsymbol{h} \cdot \nabla\mu \, dV = \int_\Omega \left[\mu \nabla \cdot \boldsymbol{h} - \nabla \cdot (\mu \boldsymbol{h}) \right] dV \, , \tag{40}$$

which can be further rewritten by inserting the continuous equation Eq. (39) and applying the divergence theorem

$$\int_\Omega \boldsymbol{h} \cdot \mathbb{M} \, dV = \int_\Omega -\mu \dot{c}^* \, dV - \int_{\partial\Omega} \mu \boldsymbol{h} \cdot \boldsymbol{n} \, dA. \tag{41}$$

Therefore, the corrosion-diffusion dissipation potential is expressed as

$$\mathfrak{D}^{ch}(\dot{c}^*, \mu, \boldsymbol{h}, \chi, \dot{\phi}_c) = \int_\Omega \left[-\mu\dot{c}^* - \chi\dot{\phi}_c - v_c^*(\mathbb{M}, \chi)\right] dV - P_{ext}^{h*}, \tag{42}$$

where P_{ext}^{h*} is the pseudo external power functional of specie flux over the entire boundary

$$P_{ext}^{h*} = \int_{\partial\Omega} \mu\boldsymbol{h}\cdot\boldsymbol{n}\, dA. \tag{43}$$

Moreover, the ductile fracture is significantly coupled with plastic deformations, and fracture and corrosion processes mutually promote each other. To capture these interactions, two coupling dissipation terms are introduced following the formulations in Miehe et al. (2016), Alessi et al. (2018)

$$\begin{aligned} &(1): \quad \mathfrak{D}^{pd}(\dot{\phi}_d) = \int_\Omega h_d' \bar{\sigma}_y \gamma \dot{\phi}_d \, dV, \\ &(2): \quad \mathfrak{D}^{dc}(\dot{\phi}_c) = \int_\Omega g_d' \gamma_d \dot{\phi}_c \, dV. \end{aligned} \tag{44}$$

In our proposed corrosion model for biodegradable magnesium alloys, we introduce a corrosion product layer between the metal and corrosive fluid. In in vitro or in vivo conditions, the stable formation of a brittle corrosion product layer on biodegradable Mg alloys hinders the transport of ions in the long-term corrosion process (Ascencio et al., 2014), resulting in diffusion-controlled corrosion (Yavuzyegit et al., 2024). Under mechanical loadings, dissolution or cracks in the corrosion product layer allow the penetration of the fluid into the surface of the Mg alloy matrix. It is noted that the diffusion of ions in the fluid is much higher than that within corrosion products. Therefore, the diffusion of ions in the cracked corrosion product layer filled with the corrosive fluid is faster than the chemical reaction within the corrosion interface. Consequently, the corrosion process transits from diffusion-controlled mode to activation-controlled mode as the corrosion layer undergoes cracking or dissolution under mechanical loadings. The effective diffusion coefficient defined in Eq. (36) captures the enhanced diffusive ability of the cracked corrosion layer. According to the coupling dissipative term in Eq. $(44)_2$, an additional driving force due to phase-field fracture also results in an acceleration of the corrosion process, which captures that the initiation and growth of microdefects under mechanical loading may increase the reaction rate through enlarging reaction area in the corrosion front (Chen et al., 2024), triggering additional microgalvanic cell reaction between the fresh-exposed damaged area and the passive film, and generating additional potential for electrochemical reactions (Huang et al., 2018; Yang et al., 2019; Liu et al., 2009).

In our model with the corrosion product layer, we combine the additional driving force term and the effective diffusion coefficient defined in Eq. (36) for the cracked corrosion product layer to capture the stress-assisted acceleration of corrosion and overcome the unphysical acceleration of the diffusion-controlled corrosion process reported in Cui et al. (2022). Neglecting this coupling between the diffusion coefficient and damage field in the corrosion layer, the additional driving force due to phase-field fracture also results in an unphysical acceleration of the diffusion-controlled corrosion process. Our coupling strategy can capture the transition of the corrosion process of biodegradable magnesium alloys from diffusion-controlled mode to activation-controlled mode under mechanical loading in physiological environments. To achieve a more general and flexible coupling between mechanical deformations and corrosion, the influence of stress and plastic deformations on the corrosion process can be introduced in the interface kinetics coefficient, which is used in Mai and Soghrati (2017), Cui et al. (2022), Kovacevic et al. (2023).

2.4. Variational principle and governing equations

With the rate of free energy $\dot{\Psi}$, the dissipation functional $\mathfrak{D}$ and the external energy functional P, the total rate-type potential functional Π from Eq. (5) is then rewritten as

$$\begin{aligned} &\Pi(\dot{\boldsymbol{u}}, \dot{\boldsymbol{\varepsilon}}^p, \dot{\gamma}, \dot{c}^*, \dot{\phi}_c, \dot{\phi}_d, \boldsymbol{s}_p, \beta, \lambda_p, \xi, \lambda_d, \mu, \chi; \boldsymbol{u}, \phi_c, \phi_d, c^*, \gamma, \boldsymbol{\varepsilon}^p) = \dot{\Psi} + \mathfrak{D} - P \\ &= \int_\Omega \Big[\boldsymbol{\sigma} : \dot{\boldsymbol{\varepsilon}} - \boldsymbol{\sigma} : \dot{\boldsymbol{\varepsilon}}^p + \sigma_\gamma \dot{\gamma} + \sigma_f \dot{\phi}_d + \sigma_{\phi_c} \dot{\phi}_c + \sigma_c \dot{c}^* + \boldsymbol{s}_p : \dot{\boldsymbol{\varepsilon}}^p - \beta\dot{\gamma} - \lambda_p(\sqrt{\frac{3}{2}}\|\mathrm{dev}[\boldsymbol{s}_p]\| - \beta - \sigma_y) \\ &+ h_d'\bar{\sigma}_y\gamma\dot{\phi}_d + \xi\dot{\phi}_d - \lambda_d(\xi - r_f) + g_d'\gamma_d\dot{\phi}_c - \mu\dot{c}^* - \chi\dot{\phi}_c - \frac{1}{2}M_c\nabla\mu\cdot\nabla\mu - \frac{L_c}{2}\left(r_c - \chi\right)^2 \\ &- \mathbf{b}\cdot\dot{\mathbf{u}} \Big] \, dV + \int_{\partial\Omega} \kappa\nabla c^*\cdot\boldsymbol{n}\dot{c}^* \, dA - \int_{\partial\Omega_{\boldsymbol{u}}^t} \bar{\boldsymbol{t}}\cdot\dot{\mathbf{u}} \, dA - \int_{\partial\Omega_{c^*}^{t_c}} \bar{t}_c\cdot\boldsymbol{n}\dot{c}^* \, dA - \int_{\partial\Omega_\mu^h} \mu\bar{\boldsymbol{h}}\cdot\boldsymbol{n} \, dA. \end{aligned} \tag{45}$$

For convenience, an associated extend argument array is defined

$$\mathfrak{a} := \{\dot{\boldsymbol{u}}, \dot{\boldsymbol{\varepsilon}}^p, \dot{\gamma}, \dot{\phi}_d, \boldsymbol{s}_p, \beta, \lambda_p, \xi, \lambda_d, \dot{c}^*, \mu, \chi, \dot{\phi}_c\}. \tag{46}$$

In addition, we write the constitutive state vector for the multifield problem

$$\mathfrak{c}^* := \{\nabla_s\boldsymbol{u}, \boldsymbol{\varepsilon}^p, \gamma, \phi_d, \phi_c, c^*, \mu, \mathbb{M}\}. \tag{47}$$

In this context, one obtains the governing equations of the fracture-corrosion system based the extended variational principle

$$\mathfrak{a} = \arg\{\underset{\mathfrak{a};\lambda_p\geq 0,\lambda_d\geq 0}{\mathrm{stat}} \Pi\}. \tag{48}$$

The necessary condition for the above principle reads $\delta\Pi \in 0$ with

$$\begin{aligned}\delta\Pi = \int_\Omega \Big[& -(\mathrm{div}\boldsymbol{\sigma} + \boldsymbol{b}) \cdot \delta\dot{\boldsymbol{u}} - (\boldsymbol{\sigma} - \boldsymbol{s}_p) : \delta\dot{\boldsymbol{\varepsilon}}^p + (\sigma_\gamma - \beta)\delta\dot{\gamma} + (\sigma_f + h_d'\bar{\sigma}_y\gamma + \xi)\delta\dot{\phi}_d - \left(\dot{\phi}_c + L_c\left(\chi - r_c\right)\right)\delta\chi \\ & + (\sigma_{\phi_c} + g_d'\gamma_d - \chi)\delta\dot{\phi}_c + (\sigma_c - \mu)\delta\dot{c}^* + (-\dot{c}^* + \nabla\cdot M_c\nabla\mu)\delta\mu + (\dot{\gamma} - \lambda_p)\delta\beta + (\dot{\phi}_d - \lambda_d)\delta\xi \\ & - \Big(\sqrt{\frac{3}{2}}\|\mathrm{dev}[\boldsymbol{s}_p]\| + \beta - \sigma_y\Big)\delta\lambda_p - (\xi - r_f)\delta\lambda_d + \Big(\dot{\boldsymbol{\varepsilon}}^p - \sqrt{\frac{3}{2}}\lambda_p\frac{\mathrm{dev}[\boldsymbol{s}_p]}{\|\mathrm{dev}[\boldsymbol{s}_p]\|}\Big) : \delta\boldsymbol{s}_p \Big]\, dV \\ & + \int_{\partial\Omega_{\boldsymbol{u}}^t}\left(\boldsymbol{\sigma}\boldsymbol{n} - \bar{\boldsymbol{t}}\right)\cdot\delta\dot{\boldsymbol{u}}\, dA + \int_{\partial\Omega_s}\alpha_c\nabla\phi_c\cdot\boldsymbol{n}\delta\dot{\phi}_c\, dA + \int_{\partial\Omega_{c^*}^{t_c}}\left(\kappa\nabla c^* - \bar{t}_c\right)\cdot\boldsymbol{n}\delta\dot{c}^*\, dA \\ & - \int_{\partial\Omega_\mu^h}(M_c\nabla\mu + \bar{h})\cdot\boldsymbol{n}\delta\mu\, dA.\end{aligned} \tag{49}$$

The variation of the functional with respect to the thirteen variables for the rates of primary fields and dissipative forces renders the coupled governing equations

$$\begin{array}{llll} (1): & \delta_{\dot{\boldsymbol{u}}}\Pi & \equiv \mathrm{div}\boldsymbol{\sigma} + \boldsymbol{b} & =0 \\ (2): & \delta_{\dot{\boldsymbol{\varepsilon}}^p}\Pi & \equiv -\boldsymbol{\sigma} + \boldsymbol{s}_p & =0 \\ (3): & \delta_{\dot{\gamma}}\Pi & \equiv \sigma_\gamma - \beta & =0 \\ (4): & \delta_{\dot{\phi}_d}\Pi & \equiv \sigma_f + h_d'\bar{\sigma}_y\gamma + \xi & =0 \\ (5): & \delta_{\dot{\phi}_c}\Pi & \equiv \sigma_{\phi_c} + g_d'\gamma_d - \chi & =0 \\ (11): & \delta_{\boldsymbol{s}_p}\Pi & \equiv \dot{\boldsymbol{\varepsilon}}^p - \sqrt{\frac{3}{2}}\lambda_p\frac{\mathrm{dev}[\boldsymbol{s}_p]}{\|\mathrm{dev}[\boldsymbol{s}_p]\|} & =0 \end{array} \qquad \begin{array}{llll} (6): & \delta_\chi\Pi & \equiv \dot{\phi}_c + L_c\left(\chi - r_c\right) & =0 \\ (7): & \delta_{\dot{c}^*}\Pi & \equiv \sigma_c - \mu & =0 \\ (8): & \delta_\mu\Pi & \equiv -\dot{c}^* + \nabla\cdot M_c\nabla\mu & =0 \\ (9): & \delta_\beta\Pi & \equiv \dot{\gamma} - \lambda_p & =0 \\ (10): & \delta_\xi\Pi & \equiv \dot{\phi}_d - \lambda_d & =0 \end{array}, \tag{50}$$

and the KKT (Karush-Kuhn–Tucker) conditions associated with the optimisation problem with inequality constraints

$$\begin{array}{llllllll} \delta_{\lambda_p}\Pi: & (1): & \lambda_p \geq 0 & (2): & \sqrt{\frac{3}{2}}\|\mathrm{dev}[\boldsymbol{s}_p]\| - \beta - \sigma_y \leq 0 & (3): & \lambda_p\left(\sqrt{\frac{3}{2}}\|\mathrm{dev}[\boldsymbol{s}_p]\| - \beta - \sigma_y\right) = 0 \\ \delta_{\lambda_d}\Pi: & (4): & \lambda_d \geq 0 & (5): & \xi - r_f \leq 0 & (6): & \lambda_d\left(\xi - r_f\right) = 0 \end{array}, \tag{51}$$

as well as the boundary conditions in the domain Ω

$$\begin{array}{llllllllll} (1): & \boldsymbol{\sigma}\boldsymbol{n} = \bar{\boldsymbol{t}} & \text{on} & \partial\Omega_{\boldsymbol{u}}^t & (2): & \mathbf{u} = \bar{\mathbf{u}} & \text{on} & \partial\Omega_{\boldsymbol{u}}^u & (3): & \nabla\phi_d\cdot\boldsymbol{n} = 0 \quad \text{on} \quad \partial\Omega \\ (4): & \phi_c = 0 & \text{on} & \partial\Omega_l & (5): & \nabla\phi_c\cdot\boldsymbol{n} = 0 & \text{on} & \partial\Omega_s & (6): & c^* = \bar{c} \quad \text{on} \quad \partial\Omega_{c^*}^c \\ (7): & \kappa\nabla c^* = \bar{t}_c & \text{on} & \partial\Omega_{c^*}^{t_c} & (8): & \mu = \bar{\mu} & \text{on} & \partial\Omega_\mu^\mu & (9): & -M_c\nabla\mu = \bar{h} \quad \text{on} \quad \partial\Omega_\mu^h \end{array}. \tag{52}$$

From governing equation system Eq. (50), the elimination of all local fields with $\boldsymbol{s}_p = -\boldsymbol{\sigma}$, $\beta = \sigma_\gamma$, $\xi = -\sigma_f - h_d'\bar{\sigma}_y\gamma$, $\chi = \sigma_{\phi_c} + g_d'\gamma_d$, $\lambda_p = \dot{\gamma}$ and $\lambda_d = \dot{\phi}_d$ yields the reduced equation system

$$\begin{array}{llllll} (1): & \mathrm{div}\boldsymbol{\sigma} + \boldsymbol{b} = 0 & (2): & \dot{\phi}_c = -L_c\left(\sigma_{\phi_c} + g_d'\gamma_d - r_c\right) & (3): & \dot{c}^* = \nabla\cdot M_c\nabla\mu \\ (4): & \dot{\gamma} \geq 0 & (5): & \sqrt{\frac{3}{2}}\|\mathrm{dev}[\boldsymbol{\sigma}]\| - \sigma_\gamma - \sigma_y \leq 0 & (6): & \dot{\gamma}\left(\sqrt{\frac{3}{2}}\|\mathrm{dev}[\boldsymbol{\sigma}]\| - \sigma_\gamma - \sigma_y\right) = 0 \\ (7): & \dot{\phi}_d \geq 0 & (8): & -\sigma_f - h_d'\bar{\sigma}_y\gamma - g_d\delta_{\phi_d}\gamma_d \leq 0 & (9): & \dot{\phi}_d\left(-\sigma_f - h_d'\bar{\sigma}_y\gamma - r_f\right) = 0 \\ (10): & \mu = \sigma_c & (11): & \dot{\boldsymbol{\varepsilon}}^p - \sqrt{\frac{3}{2}}\dot{\gamma}\frac{\mathrm{dev}[\boldsymbol{\sigma}]}{\|\mathrm{dev}[\boldsymbol{\sigma}]\|} = 0 & & \end{array}. \tag{53}$$

Eq. $(53)_{11}$ shows that the plastic strain rate $\dot{\boldsymbol{\varepsilon}}^p$ and the deviatoric stress $\mathrm{dev}[\boldsymbol{\sigma}]$ are coaxial. Thus, one obtains the relations

$$\frac{\dot{\boldsymbol{\varepsilon}}^p}{\|\dot{\boldsymbol{\varepsilon}}^p\|} = \frac{\mathrm{dev}[\boldsymbol{\sigma}]}{\|\mathrm{dev}[\boldsymbol{\sigma}]\|} \quad \text{and} \quad \dot{\gamma} = \sqrt{\frac{2}{3}}\|\dot{\boldsymbol{\varepsilon}}^p\|. \tag{54}$$

Due to the assumption of plastic incompressibility, the trace of plastic strain $tr(\boldsymbol{\varepsilon}^p)$ is equal to 0 and its deviatoric component is identical to itself $\dot{\boldsymbol{\varepsilon}}_D^p = \dot{\boldsymbol{\varepsilon}}^p$. The second term in the rate of free energy functional of Eq. (21) can then be also expressed as

$$\boldsymbol{\sigma} : \dot{\boldsymbol{\varepsilon}}^p = \mathrm{dev}[\boldsymbol{\sigma}] : \dot{\boldsymbol{\varepsilon}}^p = 2G\boldsymbol{\varepsilon}_D^e : \dot{\boldsymbol{\varepsilon}}^p. \tag{55}$$

Considering the loading and unloading processes, fracture KKT conditions in Eq. $(53)_{7-9}$ result in

$$-h_d'\left(\bar{\psi}^{ep+} + \bar{\sigma}_y\gamma\right)\begin{cases} = r_f & \text{for } \dot{\phi}_d > 0 \\ < r_f & \text{for } \dot{\phi}_d = 0 \end{cases}. \tag{56}$$

To ensure the irreversibility condition for the crack evolution equations, a local history maximum driving energy is introduced following Borden et al. (2016)

$$\mathcal{H} := \max_{\tau\in[0,t]}\left(\bar{\psi}^{ep+} + \bar{\sigma}_y\gamma\right). \tag{57}$$

Substituting $\bar{\psi}^{ep+} + \bar{\sigma}_y\gamma$ with $\mathcal{H}$, the evolution equation Eq. (56) for crack phase-field can be rewritten as

$$-h_d'\mathcal{H} + \frac{g_d}{l_d}(l_d^2\Delta\phi_d - \phi_d) = 0. \tag{58}$$

In Dittmann et al. (2018), the critical fracture energy is decreased by the total plastic work. Accordingly, we propose the degradation function for the critical energy of uncorroded material and totally corroded material g_{dm} and g_{dc} as following

$$g_{dm} := g_{dm\infty} + (g_{dm0} - g_{dm\infty})\exp(-(\gamma/\gamma_{crit})^{m_p}) \text{ and } g_{dc} := g_{dc\infty} + (g_{dc0} - g_{dc\infty})\exp(-(\gamma/\gamma_{crit})^{m_p}), \tag{59}$$

where γ_{crit} is the critical value of the equivalent accumulative plastic strain for effects of plastic deformations, and m_p is the model parameter associated with the equivalent plastic strain γ. Therein, subscripts 0 and ∞ indicate the values of critical energy taken at the elastic and saturated stages, respectively.

It is worthwhile to note that the evolution equation for concentration field Eq. $(53)_3$ is reduced to the Fick's second law

$$\int_\Omega \dot{c}^*\, dV = \int_\Omega \nabla\cdot\nabla c^*\, dA \tag{60}$$

in the pure diffusion process ($\kappa = 0$ and $\nabla\phi_c = 0$).

In the current phase field model, α_c and ω_c are correlated to the critical corrosion energy g_c and its thickness l_c of the anodic dissolution models following (Kim et al., 1999; Abubakar et al., 2015)

$$g_c = \sqrt{\frac{\omega_c\alpha_c}{18}}, \quad \text{and} \quad l_c = \alpha^*\sqrt{\frac{2\alpha_c}{\omega_c}}, \tag{61}$$

where $\alpha^* \approx 2.94$ corresponds to the transition zone taken within the range $0.05 < \phi_c < 0.95$. By evaluating the governing equations of corrosion phase-field Eq. $(53)_2$, concentration field Eq. $(53)_3$ and chemical potential Eq. $(53)_{10}$, only one of the Laplacian terms ($\Delta\phi_c$ or Δc^*) is sufficient to approximate the topology of corrosion interface, κ is assumed to be 0 for simplicity. Then, boundary condition $\bar{\boldsymbol{t}}_c\cdot\boldsymbol{n} = \kappa\nabla c^* = 0$ holds on $\partial\Omega^{t_c}_{c^*}$. Therefore, the governing equation Eq. $(53)_{10}$ is reduced to the local equation

$$\mu = 2Ac^* + 2A(c^*_{Le} - 1)(3\phi_c^2 - 2\phi_c^3) - 2Ac^*_{Le}, \tag{62}$$

and boundary conditions $\bar{c}$ on $\partial\Omega^c$ can be eliminated. The boundary conditions are reduced to

$$\begin{array}{llllllllll} (1): & \boldsymbol{\sigma n} = \bar{\boldsymbol{t}} & \text{on} & \partial\Omega^t_{\boldsymbol{u}} & (2): & \mathbf{u} = \bar{\mathbf{u}} & \text{on} & \partial\Omega^u_{\boldsymbol{u}} & (3): & \nabla\phi_d\cdot\boldsymbol{n} = 0 \quad \text{on} \quad \partial\Omega \\ (4): & \phi_c = 0 & \text{on} & \partial\Omega_l & (5): & \nabla\phi_c\cdot\boldsymbol{n} = 0 & \text{on} & \partial\Omega_s & (6): & \mu = \bar{\mu} \quad \text{on} \quad \partial\Omega^\mu_\mu \\ (7): & \boldsymbol{h} = \bar{\boldsymbol{h}} & \text{on} & \partial\Omega^{\boldsymbol{h}}_\mu & & & & & & \end{array}. \tag{63}$$

Considering the corrosion process of the magnesium alloy in physiological conditions, the initial short stage is activation-controlled due to electrochemical reactions. As the corrosion layer forms on the surface, the corrosion behaviour transits to a diffusion-controlled mode and is primarily governed by the integrity of the partly protective corrosion layer, which is revealed by the long-term in vitro corrosion experiments in Nachtsheim et al. (2022, 2024). If the corrosion layer is converted into highly soluble $MgCl_2$ or fractured under mechanical loadings, the corrosion mode transits to be activation-controlled. The present model uses the coupling term in the dissipation functional and the degradation of fracture toughness to capture the transition of corrosion modes under mechanical loadings. In summary, the current model elucidates the following interrelated couplings within the deformation-fracture-corrosion process: (1) elastic–plastic deformation energy acts as a driving force for fracture; (2) accumulated plastic deformations reduce the critical fracture energy; (3) fracture process contributes to the driving force of the corrosion field; (4) corrosion leads to a degradation of the material's critical fracture energy; and (5) the presence of cracks can accelerate the ion diffusion rate.

3. Incremental variational formulation and finite element discretisation

3.1. Time-discrete formulation

In this section,we present the finite element formulation for solving the coupled chemomechanical transient problem in a weak form. Firstly, we discretise the time interval $[0, T]$ as $\{0, t_1, t_2, \dots, t_n, t_{n+1}\}$ and focus on the finite time interval $[t_n, t_{n+1}]$ with time increment $\tau = t_{n+1} - t_n$. Assuming all state variables at time t_n are known, we update state variables at current time t_{n+1} based on the incremental variational principle (Miehe et al., 2014). Then, the extended argument array $\mathfrak{a}$ is split into an array $\{\mathfrak{m}^{n+1} - \mathfrak{m}^n\}$ involving all macroscopic/microscopic motions and an array $\mathfrak{f}$ containing the dissipative forces and Lagrange multipliers as

$$\mathfrak{m} := \{\boldsymbol{u}, \boldsymbol{\varepsilon}^p, \gamma, \phi_d, c^*, \mu, \phi_c\} \quad \text{and} \quad \mathfrak{f} := \{\boldsymbol{s}_p, \beta, \lambda_p, \xi, \lambda_d, \chi\}. \tag{64}$$

For a clearer notation, we neglect the superscript $n+1$ of all variables at time t_{n+1} in following formulations. We write the total time-discrete incremental potential functional

$$\begin{aligned} &\Pi^\tau(\mathfrak{m}, \mathfrak{f}; \mathfrak{m}^n) = \Psi - \Psi^n + \tau\mathfrak{D} - \tau P \\ &= \int_\Omega \Big[\psi^{ep}(\boldsymbol{\varepsilon}, \boldsymbol{\varepsilon}^p, \gamma, \phi_d) + \psi^{ch}(\phi_c, c^*) - \psi^{ep}(\boldsymbol{\varepsilon}^n, \boldsymbol{\varepsilon}^{pn}, \gamma^n, \phi_d^n) - \psi^{ch}(\phi_c^n, c^{*n}) + \boldsymbol{s}_p : (\boldsymbol{\varepsilon}^p - \boldsymbol{\varepsilon}^{pn}) \\ &- \beta(\gamma - \gamma^n) - \tau\lambda_p(\sqrt{\frac{3}{2}}\|\mathrm{dev}[\boldsymbol{s}_p]\| - \beta - h_d\bar{\sigma}_y) + \xi(\phi_d - \phi_d^n) - \tau\lambda_d(\xi - r_f) - \mu(c^* - c^{*n}) \\ &- \chi(\phi_c - \phi_c^n) - \tau\frac{M_c}{2}\nabla\mu\cdot\nabla\mu - \tau\frac{L_c}{2}(r_c - \chi)^2 + h'_d\bar{\sigma}_y\gamma(\phi_d - \phi_d^n) + g'_d\gamma_d(\phi_c - \phi_c^n) - \boldsymbol{b}\cdot(\boldsymbol{u} - \boldsymbol{u}^n) \Big]\, dV \\ &- \int_{\partial\Omega^t_{\boldsymbol{u}}} \bar{\boldsymbol{t}}\cdot(\mathbf{u} - \mathbf{u}^n)\, dA - \int_{\partial\Omega^{t_c}_{c^*}} \bar{\boldsymbol{t}}_c\cdot\boldsymbol{n}(c^* - c^{*n})\, dA - \int_{\partial\Omega^h_\mu} \tau\mu\bar{\boldsymbol{h}}\cdot\boldsymbol{n}\, dA, \end{aligned} \tag{65}$$

where $\bar{t}_c = 0$ holds. The time-discrete extended arguments $\{\mathfrak{m}, \mathfrak{f}\}$ at time t_{n+1} is obtained by finite-step-sized incremental variational principle

$$\{\mathfrak{m}, \mathfrak{f}\} = \arg\{\operatorname*{stat}_{\{\mathfrak{m},\mathfrak{f}\};\lambda_p\geq 0,\lambda_d\geq 0} \Pi^\tau\}, \tag{66}$$

for which the necessary condition reads $\delta\Pi^\tau \in 0$.

3.2. Condensation of local fields

Considering the local terms in the potential functional, the saddle point statement Eq. (66) can be solved split within an two-step algorithm. Firstly, the local variables $\{\boldsymbol{\varepsilon}^p, \gamma, c^*, \boldsymbol{s}_p, \beta, \lambda_p, \xi, \lambda_d, \chi\}$ are obtained for given global fields $\{\boldsymbol{u}, \phi_d, \phi_c, \mu\}$ by the local saddle point statement

$$\{\boldsymbol{\varepsilon}^p, \gamma, c^*, \boldsymbol{s}_p, \beta, \lambda_p, \xi, \lambda_d, \chi\} = \arg\{\operatorname*{stat}_{\{\boldsymbol{\varepsilon}^p,\gamma,c^*,\boldsymbol{s}_p,\beta,\lambda_p,\xi,\lambda_d,\chi;\lambda_p\geq 0,\lambda_d\geq 0\}} \Pi^\tau\}, \tag{67}$$

which results in the update formulas

$$\begin{array}{llllllll}
(1): & \delta_{\boldsymbol{\varepsilon}^p}\Pi^\tau & \equiv \boldsymbol{\sigma} - \boldsymbol{s}_p & = 0 & (2): & \delta_\gamma \Pi^\tau & \equiv \sigma_\gamma - \beta & = 0 \\
(3): & \delta_{\boldsymbol{s}_p}\Pi^\tau & \equiv \boldsymbol{\varepsilon}^p - \boldsymbol{\varepsilon}^{pn} - \tau\sqrt{\frac{3}{2}}\lambda_p \frac{\operatorname{dev}[\boldsymbol{s}_p]}{\|\operatorname{dev}[\boldsymbol{s}_p]\|} & = 0 & (4): & \delta_{c^*}\Pi^\tau & \equiv \sigma_c - \mu & = 0 \\
(5): & \delta_\beta \Pi^\tau & \equiv \gamma - \gamma^n - \tau\lambda_p & = 0 & (6): & \delta_\chi \Pi^\tau & \equiv -\phi_c + \phi_c^n + \tau L_c(r_c - \chi) & = 0 \\
(7): & \delta_\xi \Pi^\tau & \equiv \phi_d - \phi_d^n - \tau\lambda_d & = 0 & & & &
\end{array} \tag{68}$$

$$\begin{array}{llllll}
\delta_{\lambda_p}\Pi^\tau: & (1): & \tau\lambda_p \geq 0 & (2): & \sqrt{\frac{3}{2}}\|\operatorname{dev}[\boldsymbol{s}_p]\| - \beta - \sigma_y \leq 0 & (3): \quad \tau\lambda_p\left(\sqrt{\frac{3}{2}}\|\operatorname{dev}[\boldsymbol{s}_p]\| - \beta - \sigma_y\right) = 0 \\
\delta_{\lambda_d}\Pi^\tau: & (4): & \tau\lambda_d \geq 0 & (5): & \xi - r_f \leq 0 & (6): \quad \tau\lambda_d\left(\xi - r_f\right) = 0
\end{array}, \tag{69}$$

In the current step, the trial stress predictor $\boldsymbol{\sigma}^{pr}$ is initially calculated based on the return mapping algorithm

$$\boldsymbol{\sigma}^{pr} = \boldsymbol{\sigma}^n + \mathbb{C}^e \Delta\boldsymbol{\varepsilon}, \tag{70}$$

where $\mathbb{C}^e$ is the fourth-order elastic constitutive Jacobian tensor and defined by

$$[\mathbb{C}^e]_{ijkl} = K\delta_{ij}\delta_{kl} + h_d\bar{G}(\delta_{ik}\delta_{jl} + \delta_{il}\delta_{jk} - \frac{2}{3}\delta_{ij}\delta_{kl}), \text{ with } K = \begin{cases} h_d\bar{K} & \text{for } \operatorname{tr}(\boldsymbol{\varepsilon} - \boldsymbol{\varepsilon}^{pn}) \geq 0 \\ \bar{K} & \text{for } \operatorname{tr}(\boldsymbol{\varepsilon} - \boldsymbol{\varepsilon}^{pn}) < 0 \end{cases}. \tag{71}$$

With the stress predictor in hand we write the trial yield function from Eqs. $(68)_{1,2}$ and $(69)_2$

$$f_p^{pr} = \sqrt{\frac{3}{2}}\|\operatorname{dev}[\boldsymbol{\sigma}^{pr}]\| - H\gamma^n - \sigma_y \tag{72}$$

Subsequently, the accumulative plastic strain is updated following

$$\gamma = \begin{cases} \frac{\sqrt{\frac{3}{2}}\|\operatorname{dev}[\boldsymbol{\sigma}^{pr}]\| - \sigma_y}{3G+H} & \text{for } f_p^{pr} > 0 \\ \gamma^n & \text{for } f_p^{pr} \leq 0 \end{cases}. \tag{73}$$

The reformulation of Eqs. $(68)_{1,3,5}$ provides the linear update formula of the plastic strain tensor

$$\boldsymbol{\varepsilon}^p - \boldsymbol{\varepsilon}^{pn} = \sqrt{\frac{3}{2}}(\gamma - \gamma^n)\hat{\boldsymbol{n}} \quad \text{and} \quad \hat{\boldsymbol{n}} = \frac{\operatorname{dev}[\boldsymbol{\sigma}^{pr}]}{\|\operatorname{dev}[\boldsymbol{\sigma}^{pr}]\|}. \tag{74}$$

Regarding the corrosion-related equations, Eq. $(68)_4$ are used to calculate the local concentration c^* by combining Eq. (62), while the local dissipative force χ dual to the corrosion phase-field is updated by using Eq. $(68)_6$, where the corrosion energy r_c is computed with Eq. (37). The fracture-related local equations, Eq. $(68)_7$ and Eqs. $(69)_{1-3}$, lead to the evolution equation of fracture dissipative force ξ, as

$$\xi \begin{cases} = r_f & \text{for } \phi_d > \phi_d^n \\ < r_f & \text{for } \phi_d = \phi_d^n \end{cases}, \tag{75}$$

where the fracture dissipative resistance r_f is computed with using Eq. (29). It is emphasised that the dissipative force-like terms, $h_d'\bar{\sigma}_y\gamma$ and $g_d'\gamma_d$, in the incremental dissipation potential are also calculated locally.

3.3. Staggered algorithm and finite element discretisation

By utilising the local stationary principle in Eq. (68), we define the reduced global algorithmic functional

$$\begin{aligned}\Pi^{\tau}_{red}(\boldsymbol{u},\phi_d,\phi_c,\mu) = \int_{\Omega} \Big[\, \psi(\boldsymbol{\varepsilon},\phi_d,\phi_c) - \psi^n + r_f(\phi_d-\phi_d^n) - \mu(c^*-c^{*n}) - \tau\frac{M_c}{2}\nabla\mu\cdot\nabla\mu - r_c(\phi_c-\phi_c^n) \\ + \frac{(\phi_c-\phi_c^n)^2}{2\tau L_c} + h_d'\bar{\sigma}_y\gamma(\phi_d-\phi_d^n) + g_d'\gamma_d(\phi_c-\phi_c^n) - \boldsymbol{b}\cdot(\boldsymbol{u}-\boldsymbol{u}^n)\,\Big]\, dV - \int_{\partial\Omega^t_u}\bar{\boldsymbol{t}}\cdot(\mathbf{u}-\mathbf{u}^n)\,dA \\ - \int_{\partial\Omega^h_\mu}\tau\mu\bar{\boldsymbol{h}}\cdot\boldsymbol{n}\,dA.\end{aligned} \tag{76}$$

Then, the second step for solving global variables is based on the global saddle point statement

$$\{\boldsymbol{u},\phi_d,\phi_c,\mu\} = \arg\{\inf_{\boldsymbol{u}}\inf_{\phi_d}\inf_{\phi_c}\sup_{\mu}\Pi^{\tau}_{red}\}, \tag{77}$$

resulting in the weak form of global governing equations

$$\delta\Pi^{\tau}_{red}[\delta\boldsymbol{u}] = \int_{\Omega}\left(\boldsymbol{\sigma}:\delta\nabla_s\boldsymbol{u} - \boldsymbol{b}\cdot\delta\boldsymbol{u}\right)dV - \int_{\partial\Omega^t_u}\bar{\boldsymbol{t}}\cdot\delta\boldsymbol{u}\,dA = 0, \tag{78}$$

$$\delta\Pi^{\tau}_{red}[\delta\phi_d] = \int_{\Omega}\left(h_d'\bar{\psi}^{ep+}\delta\phi_d + h_d'\bar{\sigma}_y\gamma\delta\phi_d + r_f\delta\phi_d\right)dV = 0, \tag{79}$$

$$\delta\Pi^{\tau}_{red}[\delta\phi_c] = \int_{\Omega}\left(\sigma_{\phi_c}\delta\phi_c - r_c\delta\phi_c + \frac{\phi-\phi^n}{\tau L_c}\delta\phi_c + g_d'\gamma_d\delta\phi_c\right)dV = 0, \tag{80}$$

$$\delta\Pi^{\tau}_{red}[\delta\mu] = \int_{\Omega}\left[-(c^*-c^{*n})\delta\mu - \tau M_c\nabla\mu\cdot\delta\nabla\mu\right]dV - \int_{\partial\Omega^h_\mu}\tau\bar{\boldsymbol{h}}\cdot\boldsymbol{n}\delta\mu\,dA = 0. \tag{81}$$

Considering a staggered algorithm, the displacement field is solved by freezing the fracture phase-field at the last increment. Meanwhile, the other three fields are solved by freezing the displacement field. As introduced in Section 2.4, KKT conditions for fracture Eq. $(69)_{4-6}$ can be reformulated into a single equation using the historical maximum energy $\mathcal{H}$. The value of $\mathcal{H}$ at time step t_{n+1} is then obtained after the update of displacement field by

$$\mathcal{H} = \begin{cases}\bar{\psi}^{ep+}(\boldsymbol{\varepsilon}) + \bar{\sigma}_y & \text{for } \bar{\psi}^{ep+}(\boldsymbol{\varepsilon}) + \bar{\sigma}_y > \mathcal{H}^n \\ \mathcal{H}^n & \text{otherwise}\end{cases}. \tag{82}$$

We merge $\mathcal{H}$ into Eq. (79) to substitute $\bar{\psi}^{ep+}+\bar{\sigma}_y\gamma$. Furthermore, we reintegrate Eqs. (29) and (37) for the definition of the dissipative resistances, r_f and r_c, into the global equations Eqs. (79) and (80). The divergence theorem is used to reduce the Laplacian terms $\nabla\cdot\nabla\phi_d$ and $\nabla\cdot\nabla\phi_c$, leading to

$$\delta\Pi^{\tau}_{red}[\delta\phi_d] = \int_{\Omega}\left(h_d'\mathcal{H}\delta\phi_d + \frac{g_d}{l_d}\phi_d\delta\phi_d + g_d l_d\nabla\phi_d\cdot\delta\nabla\phi_d\right)dV = 0, \tag{83}$$

$$\delta\Pi^{\tau}_{red}[\delta\phi_c] = \int_{\Omega}\left(\sigma_{\phi_c}\delta\phi_c + w_c g_w{}'\delta\phi_c + \alpha_c\nabla\phi_c\cdot\delta\nabla\phi_c + \frac{\phi-\phi^n}{\tau L_c}\delta\phi_c + g_d'\gamma_d\delta\phi_c\right)dV = 0. \tag{84}$$

By discretising the computational domain into N_{elem} finite elements with the volume Ω^e and the number of nodes N_{node}, the field variables are interpolated as

$$\begin{aligned}\mathbf{u} &= \sum_{i=1}^{N_{\text{node}}}\mathbf{N}_i^{\boldsymbol{u}}\mathbf{u}_i = \boldsymbol{N}^{\boldsymbol{u}}\{\boldsymbol{u}\}^e, \quad \phi_d = \sum_{i=1}^{N_{\text{node}}}N_i\phi_{d\,i} = \boldsymbol{N}\{\phi_d\}^e, \\ \phi_c &= \sum_{i=1}^{N_{\text{node}}}N_i\phi_{c\,i} = \boldsymbol{N}\{\phi_c\}^e, \quad \mu = \sum_{i=1}^{N_{\text{node}}}N_i\mu_i = \boldsymbol{N}\{\mu\}^e,\end{aligned} \tag{85}$$

where N_i denotes the shape function associated with node i. $\mathbf{N}_i^{\boldsymbol{u}}$ is a diagonal matrix with main diagonal components being N_i. Furthermore, $\{(\cdot)\}^e$ is the degree of freedom $(\cdot)$ of all nodes in an element, *e.g.* $\{\boldsymbol{u}\}^e = [\boldsymbol{u}_1,\boldsymbol{u}_2,\dots,\boldsymbol{u}_i,\dots,\boldsymbol{u}_{N_{\text{node}}}]^T$. Using the Voigt notation for symmetric second order tensors, the corresponding derivatives can be computed as:

$$\boldsymbol{\varepsilon} = \mathbf{B}^{\boldsymbol{u}}\{\mathbf{u}\}^e, \quad \nabla\phi_d = \mathbf{B}\{\phi_d\}^e, \quad \nabla\phi_c = \mathbf{B}\{\phi_c\}^e, \quad \nabla\mu = \mathbf{B}\{\mu\}^e, \tag{86}$$

where $\mathbf{B}^{\boldsymbol{u}}$ and $\mathbf{B}$ are the spatial derivative matrices corresponding to $\boldsymbol{N}^{\boldsymbol{u}}$ and $\boldsymbol{N}$. Inserting the nodal displacement variables, weak form Eqs. (78), (83), (81) and (84) give the discretised residuals

$$\boldsymbol{R}_{\boldsymbol{u}} = \mathop{\mathbf{A}}_{e=i}^{N_{elem}}\int_{\Omega^e}\left((\mathbf{B}^{\boldsymbol{u}})^T\boldsymbol{\sigma} - (\mathbf{N}^{\boldsymbol{u}})^T\boldsymbol{b}\right)dV - \mathop{\mathbf{A}}_{e=i}^{N_{elem}}\int_{\partial(\Omega^e)^t_{\boldsymbol{u}}}(\mathbf{N}^{\boldsymbol{u}})^T\bar{\boldsymbol{t}}dA, \tag{87}$$

$$\boldsymbol{R}_{\phi_d} = \mathop{\mathbf{A}}_{e=i}^{N_{elem}}\int_{\Omega^e}\left(h_d'\mathcal{H}\boldsymbol{N} + \frac{g_d}{l_d}\boldsymbol{N}^T\phi_d + g_d l_d\mathbf{B}^T\nabla\phi_d\right)dV, \tag{88}$$

$$\boldsymbol{R}_{\phi_c} = \mathop{\mathbf{A}}_{e=i}^{N_{elem}}\int_{\Omega^e}\left(\frac{\phi_c-\phi_c^n}{\tau L_c}\boldsymbol{N} + \sigma_{\phi_c}\boldsymbol{N} + g_d'\gamma_d\boldsymbol{N} + w_c g_w'\boldsymbol{N} + \alpha_c\mathbf{B}^T\nabla\phi_c\right)dV, \tag{89}$$

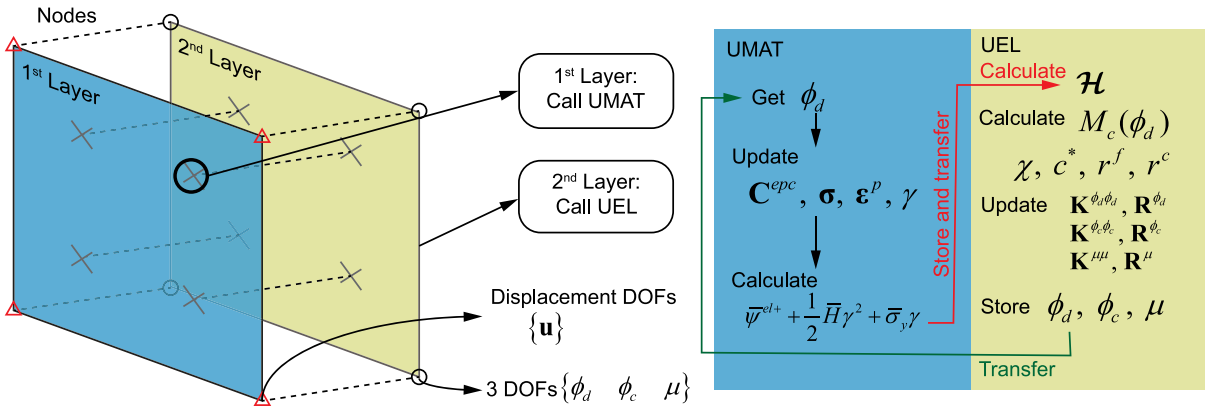

Fig. 2. Two-layer structure of finite element computations implemented in Abaqus with user-subroutines.

$$\boldsymbol{R}_{\mu} = \mathop{\mathbf{A}}_{e=i}^{N_{elem}} \int_{\Omega^e} \left(\frac{c^* - c^{*n}}{\tau} \boldsymbol{N} + M_c \mathbf{B}^T \nabla \mu \right) dV - \mathop{\mathbf{A}}_{e=i}^{N_{elem}} \int_{\partial(\Omega^e)^h_{\mu}} \left(\tau \bar{\boldsymbol{h}} \cdot \boldsymbol{n} \right) \boldsymbol{N} dA. \tag{90}$$

In the current staggered algorithm, the assumptions $\partial \boldsymbol{R}_{\boldsymbol{u}}/\partial \phi_d = \mathbf{0}$, $\partial \boldsymbol{R}_{\phi_d}/\partial \boldsymbol{u} = 0$, $\partial \boldsymbol{R}_{\phi_d}/\partial \phi_c = 0$ and $\partial \boldsymbol{R}_{\phi_c}/\partial \phi_d = 0$ are made to decouple the system of equations. Then, the update of the global state variables is achieved by the Newton–Raphson iteration procedure of the nonlinear equation system

$$\begin{Bmatrix} \boldsymbol{u} \\ \phi_d \\ \phi_c \\ \mu \end{Bmatrix} \Leftarrow \begin{Bmatrix} \boldsymbol{u} \\ \phi_d \\ \phi_c \\ \mu \end{Bmatrix} - \begin{bmatrix} \mathbf{K}^{\boldsymbol{uu}} & 0 & 0 & 0 \\ 0 & \mathbf{K}^{\phi_d \phi_d} & 0 & 0 \\ 0 & 0 & \mathbf{K}^{\phi_c \phi_c} & 0 \\ 0 & 0 & 0 & \mathbf{K}^{\mu\mu} \end{bmatrix}^{-1} \begin{Bmatrix} \boldsymbol{R}_{\boldsymbol{u}} \\ R_{\phi_d} \\ R_{\phi_c} \\ R_{\mu} \end{Bmatrix}, \tag{91}$$

where the components of tangent matrix are calculated by

$$\mathbf{K}^{\boldsymbol{uu}} = \mathop{\mathbf{A}}_{e=i}^{N_{elem}} \int_{\Omega^e} (\mathbf{B}^{\boldsymbol{u}})^T \boldsymbol{C}^{epc} \mathbf{B}^{\boldsymbol{u}} dV, \tag{92}$$

$$\mathbf{K}^{\phi_d \phi_d} = \mathop{\mathbf{A}}_{e=i}^{N_{elem}} \int_{\Omega^e} \left\{ \left(h_d'' \mathcal{H} + \frac{g_d}{l_d} \right) \boldsymbol{N}^T \boldsymbol{N} + g_d l_d \mathbf{B}^{\mathrm{T}} \mathbf{B} \right\} dV, \tag{93}$$

$$\mathbf{K}^{\phi_c \phi_c} = \mathop{\mathbf{A}}_{e=i}^{N_{elem}} \int_{\Omega^e} \left[\left(\frac{1}{\tau L_{\phi_c}} + \frac{\partial^2 \psi^{ch}}{\partial \phi_c^2} + g_d'' \gamma_d + w_c g_w'' \right) \boldsymbol{N}^T \boldsymbol{N} + \alpha_{\phi} \mathbf{B}^T \mathbf{B} \right] dV, \tag{94}$$

$$\mathbf{K}^{\mu\mu} = \mathop{\mathbf{A}}_{e=i}^{N_{elem}} \int_{\Omega^e} M_c \mathbf{B}^T \mathbf{B} dV. \tag{95}$$

$\boldsymbol{C}^{epc}$ is the consistent tangent matrix, and its corresponding fourth-order symmetric tensor $\mathbb{C}^{epc}$ is

$$\mathbb{C}^{epc} = 2Gq\mathbb{I} + (K - \frac{2}{3}Gq)\boldsymbol{I} \otimes \boldsymbol{I} + 2G(\frac{H}{3G+H} - q)\hat{\boldsymbol{n}} \otimes \hat{\boldsymbol{n}} \quad \text{with} \quad q = \frac{\|\mathrm{dev}[\boldsymbol{\sigma}]\|}{\|\mathrm{dev}[\boldsymbol{\sigma}^{pr}]\|}, \tag{96}$$

$$[\boldsymbol{C}^{epc}]_{\alpha\beta} = \zeta [\mathbb{C}^{epc}]_{ijkl} \quad \text{with} \quad \zeta = \begin{cases} 1 & \beta \in \{1,2,3\} \\ 1/2 & \beta \in \{4,5,6\} \end{cases}, \quad \begin{array}{|c|cccc|} \hline \alpha \leftarrow ij & 1 \leftarrow 11 & 2 \leftarrow 22 & 3 \leftarrow 33 \\ \beta \leftarrow kl & 4 \leftarrow 12 & 5 \leftarrow 13 & 6 \leftarrow 23 \\ \hline \end{array}, \tag{97}$$

where $\mathbb{I}$ is the fourth-order identity tensor.

The model is implemented in Abaqus through the user-defined material (UMAT) and user-defined element (UEL) subroutines as shown in Fig. 2. The FEM model contains two layers of elements sharing the same nodes and different degrees of freedom (DOFs). The first layer elements have displacement DOFs and invoke UMAT subroutine at each Gauss point, while the second layer elements are activated with 3 DOFs for fracture field, corrosion field and chemical potential and call UEL subroutine. At the beginning of time step t_{n+1}, UMAT updates the elastic–plastic response by using ϕ_d^n from the last increment, and then passes $\mathcal{H}$ stored at Gauss points to UEL. Using the staggered algorithms, the solution ϕ_d of the second layer elements in UEL is saved at this time increment and pass related results to the Gauss points in the first layer.

4. Materials and in vitro experiments

The extruded rare-earth magnesium alloy WE43MEO (Meotec GmbH, Germany) supplied by Medical Magnesium GmbH (Aachen, Germany) was used to fabricate tensile specimens with detailed geometries and dimensions shown in Fig. 3a. The chemical components are listed in Table 1. In vitro experiments were carried out in the cell culture medium Dulbecco's Modified Eagle Medium

Table 1
Chemical compositions of WE43 alloy.

Y	Nd	Zr	Al	Mn	Fe	Mg
3.8%	2.6%	0.02%	<0.01%	0.0025%	0.0065%	Bal.

Table 2
Ionic concentration in DMEM (unit in mmol/L).

Na^+	K^+	Mg^{2+}	Ca^{2+}	Cl^-	HCO_3^-	HPO_4^{2-}	SO_4^{2-}
154	5.4	0.8	1.8	119	44	1	0.8

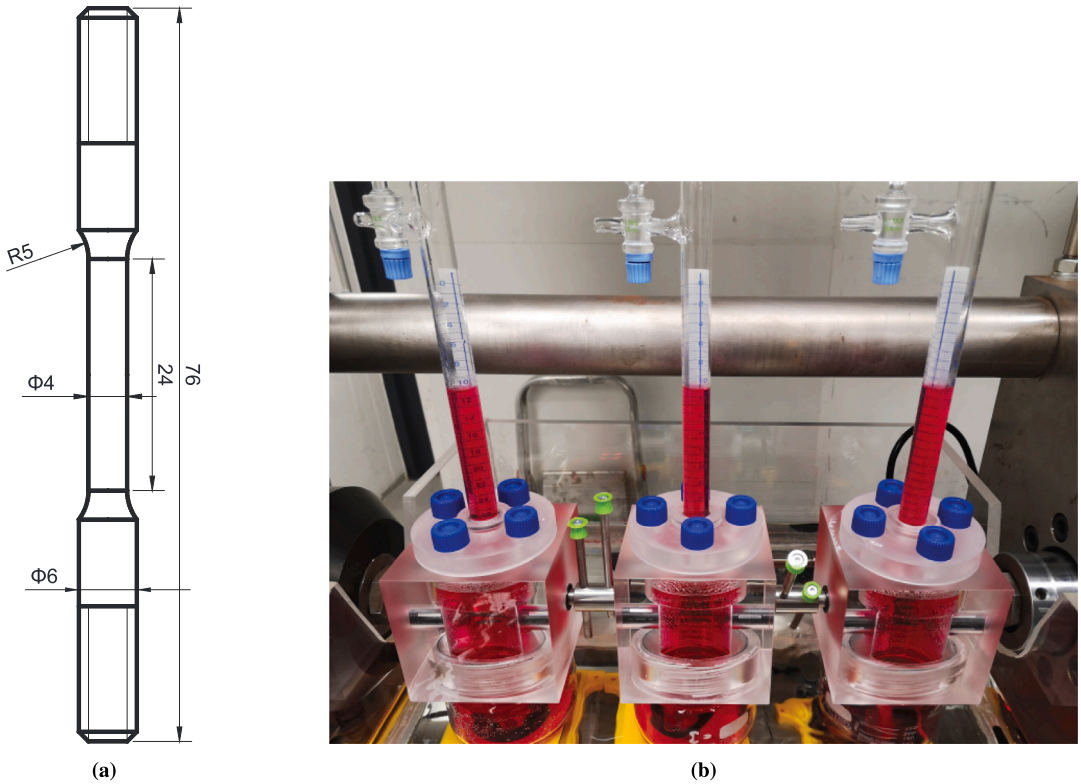

Fig. 3. In vitro experiments: (a) geometry and dimensions (unit in mm) of the smooth round WE43 specimen and (b) experimental set-up of SSRTC tests.

(DMEM, L0101-500, Biowest, Nuaillé, France), which is supplemented with Penicillin-Streptomycin and sodium azide for avoiding bacterial contamination. Dulbecco's Modified Eagle Medium is an organic cell culture medium with bio-relevant compounds, *e.g.*, amino acids, glucose, and vitamins, which is closest to human blood plasma in compositions and concentrations (Nachtsheim et al., 2022). The ionic concentration in DMEM is listed in Table 2. For detailed description of in vitro experiments the reader is referred to Nachtsheim et al. (2022, 2024).

4.1. Immersion testing

The smooth samples were prepared for immersion experiments by wrapping both ends with Teflon tape and sealing them with heat shrink tubing to prevent corrosion. This ensured that only the uniform midsection of the samples was exposed to the corrosive environment. Prior to the corrosion test, the specimens were disinfected overnight in 80% ethanol and left to dry completely. Subsequently, the ends of the samples were fixed in a funnel and immersed horizontally in the corrosion medium. The corrosion experimental apparatus was maintained at a temperature of 37 °C and 7% CO_2 to simulate the average human body environment. The pH value was kept in the physiological regime and controlled optically using the phenol red colour indicator in the DMEM fluid, and the experiments with an unphysiological pH regime or contaminations were stopped. Samples were immersed in the medium for a maximum period of 28 days. In order to remove the loose corrosion products on sample surfaces after immersion tests, the samples were removed from the medium, washed with deionised water, 80% ethanol and dried in air.

Table 3
Values of the corrosion model parameters for the pencil electrode test (Cui et al., 2021).

Parameter	Physical interpretation	Value
g_c	Critical corrosion energy	0.01 N/mm
l_c	Corrosion interface thickness	0.005 mm
D_c	Diffusion coefficient	8.5×10^{-4} mm^2/s
L_c	Interface kinetics coefficient	2×10^6 mm^2/(Ns)
A	Free energy density curvature	53.5 N/mm^2
c^*_{Le}	Normalised concentration in the saturated solution	0.035

4.2. Uniaxial tensile testing

Uniaxial tensile tests were carried out after different immersion times (0, 7, 14, 21 and 28 days). The uniaxial tensile tests were performed using an MTS Mini Bionix II servo-hydraulic testing machine, which was configured for uniaxial axial tension in accordance with the ASTM test standard. During the tests, the force applied to the samples was measured by the load cell of the testing machine, which has a capacity of 25 kN. The strain in the midsection of the specimens was recorded using GOM Aramis SRX during testing. The specimens were subjected to the displacement-controlled loading at a rate of 1 mm/min, and all tests were carried out at room temperature.

4.3. Slow strain rate tensile-corrosion testing

The stress corrosion cracking in WE43MEO magnesium alloys was investigated using slow strain rate tensile-corrosion (SSRTC) tests, as shown in Fig. 3b. In the previous experiments in Nachtsheim et al. (2022), it is observed that the highest corrosion rates occur within the immersion time of 24 h. We selected the different loading rates in the SSRTC tests to allow a corrosion period within this immersion time according to the fracture displacement of the specimen identified in the tensile test. The tests were performed under displacement control with loading rates of 0.3 mm/h, 0.1 mm/h and 0.06 mm/h, respectively. The midsection of the specimens was immersed in the medium, and both ends were fixed in the testing machine. The testing environment was maintained at 37 °C, consistent with the immersion test. The force and displacement of the end were both measured by the load cell of the test machine.

5. Computational simulations and validations

5.1. Analytical validation of uniform corrosion model: pencil electrode test

The numerical implementation in Abaqus for modelling the corrosion behaviour is validated by comparing the simulation result with the analytical result of a pencil electrode under uniform corrosion conditions. In this example schematically illustrated in Fig. 4a, a metal specimen with the radius r = 12.5 μm and the height H = 125 μm encapsulated in an epoxy coating with the top end exposed to the electrolyte. The associated boundary conditions are specified with Dirichlet conditions $\phi_c = 0$, $\mu = -2Ac^*_{Le}$ on the top end and Neumann conditions $\nabla\phi_c \cdot \boldsymbol{n} = 0$, $\boldsymbol{h} = 0$ on the other boundaries. The initial conditions of the metal specimen are defined as $\mu = 0$ and $\phi_c = 1$ at time $t = 0$. The corrosion interface evolves along the length of the specimen in a diffusion-controlled mode due to the sufficiently high chemical reaction rate, which is resulted from the used model parameters in Table 3. Furthermore, a saturated ion film can always be maintained along the interface, as seen in Fig. 4b (A and B). The analytical solution of the pencil electrode test in a diffusion-controlled mode is taken from Scheiner and Hellmich (2007), where the corrosion depth x_d given by

$$x_d = 2\xi_d\sqrt{D_c t} \quad \text{with} \quad \frac{c^*_{Le}}{1 - c^*_{Le}}\exp(-\xi_d^2) = \sqrt{\pi}\xi_d \operatorname{erf}(\xi_d). \tag{98}$$

To ensure the numerical stability and accuracy of simulations, the model is discretised using 8-node second-order axisymmetric quadrilateral elements with mesh size 1 μm. The comparison between the analytical and numerical solutions is shown in Fig. 4b. It can be seen that the numerical prediction agrees well with the analytical solution in terms of the corrosion depth.

5.2. Calibration and validation for corrosion and fracture of WE43MEO

In this section, we calibrate and validate the proposed multifield model for predicting the fracture, degradation and SCC behaviours of bioabsorbable magnesium alloys in vitro experiments. Due to the very high computational cost for the 3D simulation, we employed an axisymmetric model to compare the radius reduction of the equivalent corrosion profile from experiments and simulations. The difference of simulation results with the axisymmetric model and 3D models is shown in Appendix C. The axisymmetric finite element model is used to represent the specimen with symmetric boundary conditions, as shown in Fig. 5. For the numerical simulation of the uniaxial tensile experiment, the model is discretised using fully integrated second-order 8-node axisymmetric elements with a mesh size of 0.02 mm in the midsection of the specimen, where the corrosion and fracture are expected to occur. In the simulation, displacements of the reference point (marked as RP in Fig. 5) in the axial direction are used for plotting the force–displacement curve in the uniaxial tensile tests, while displacements of the upper boundary are used in

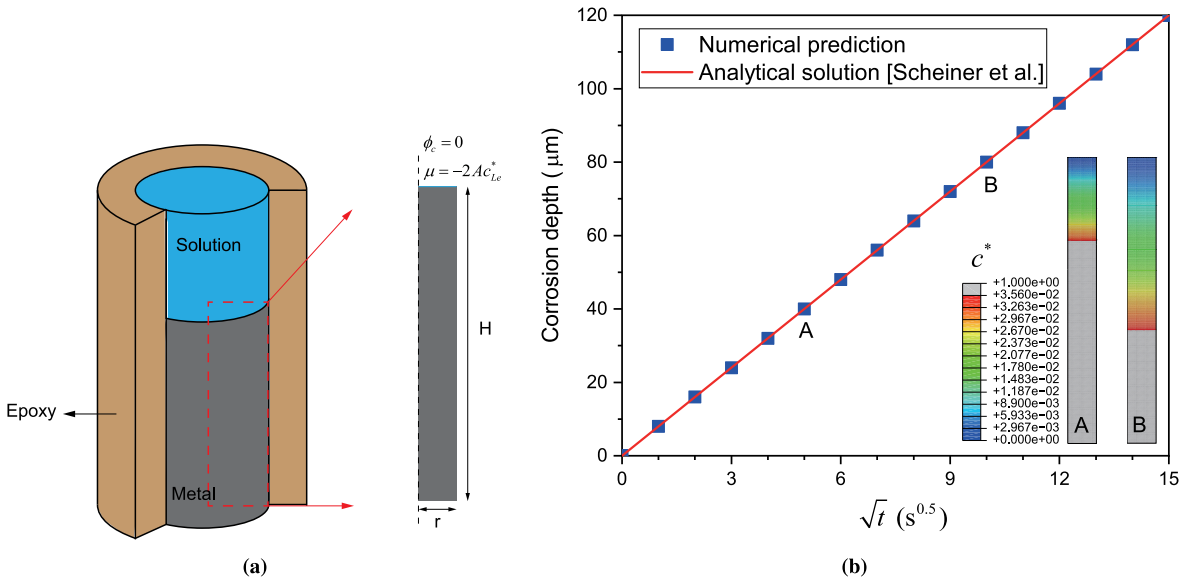

Fig. 4. Pencil electrode test: (a) schematic illustration and (b) numerical and analytical solutions for corrosion depth versus $\sqrt{t}$, and the distributions of normalised concentration at $t = 25$ s and $t = 100$ s.

SSRTC tests, according to the measurement method adopted in the experiments. The maximum allowed displacement increments are restricted to 5 μm in all simulations for achieving convergent solutions. The initial size and spacing of these pits are determined by the experimental analysis of the morphology of pits on the cross-section of the specimen specimens. After the corrosion of 7 days, the average width of the pits is approximately 200 μm. Accordingly, the initial size of pits w_{pit} is set to be 200 μm in the simulation. To consider the inhomogeneous coalescence of the pits, two spacing values, w_{pit} and $2 * w_{pit}$, between pits are used in the simulation. Correspondingly, 2 pits are assigned in 1 mm length, as shown in Fig. 5. The distributions of the pit number and size should be statistically identical in the circumferential and axial directions. Therefore, we set 20 pits with two spacings in the axial direction for the gauge length of 10 mm in the axisymmetric model. In the region of initial pits, $\mu = -2Ac^*_{Le}$ and $\phi_c = 0$ are prescribed as boundary conditions, while $\mu = 0$ and $\phi_c = 1$ are defined in the other region of specimens at time $t = 0$ as initial conditions. The boundary conditions lead to differences in corrosion field and chemical potential compared to the initial state of the Mg alloy matrix, thus triggering corrosion at these specified boundaries. As stable gradients form in the corrosion and chemical potential fields, the pits will extend both inwardly and laterally. Thus, in the simulation, corrosion pits can initiate and evolve autonomously with these boundary conditions. With these computational simulations, we demonstrate the interactions of inelastic deformations, fracture and corrosion of the WE43 Mg alloy.

The proposed model includes three sets of materials parameters, which are related to the deformation and fracture behaviour, the corrosion behaviour and the interaction between fracture and corrosion behaviours. The effective elastic constants $\bar{K}$ and $\bar{G}$ can be calculated with the Young's modulus from the uniaxial test and the Poisson ratio 0.27 (Kondori and Benzerga, 2017). The effective initial yield stress $\bar{\sigma}_y$ and the hardening modulus $\bar{H}$ are determined also from the stress–strain curve in the uniaxial test. The other model parameters γ_{crit}, g_{dm0} and m_p related to fracture behaviour are iteratively adjusted with $g_{dm\infty} = 0.15 g_{dm0}$ following (Dittmann et al., 2018) to achieve the best fit to the post-necking region of the stress–stress curve from the experiment. The saturated Mg-ion concentration in WE43 c_{solid} and totally corroded material c^*_{Le} are calculated following the work done by Shen et al. (2019). The interface thickness associated with corrosion and fracture l_c and l_d set to 0.1 mm according to the used characteristic dimension of the stress corrosion process of magnesium alloys in Gastaldi et al. (2011). Diffusion coefficient of magnesium ions in electrolyte D_{cl} is taken within the range from the literature (Lemkul and MacKerell, 2016; Höche, 2014). According to the experimental observation of in vitro corrosion experiments, the corrosion process of WE43 is dominantly diffusion-controlled due to the deposition of corrosion products on the surface. Correspondingly, the value of L_c should be sufficiently large to ensure the diffusion-controlled corrosion mode. In the slow strain rate tensile-corrosion testing, the corrosion mode transits to be activation-controlled due to the fracture of the corrosion product layer. The parameter L_c and model parameters m_d and m_c for the interaction of fracture and corrosion are determined iteratively to match the force–displacement curve of the SSRTC experiment with the loading rate 0.1 mm/h. The critical fracture energy of corroded materials g_{dc} is set to be $g_{dc} = 0.01 g_{dm0}$ as the corrosion layer becomes much brittle. The model parameters calibrated for these computational simulations are shown in Table 4.

5.2.1. *Experimental and computational results of uniaxial tensile tests*

Fig. 6a shows force–displacement curves from computational simulations and experiments of uniaxial tensile tests on uncorroded specimens. The fracture morphology in the experiments exhibits a cup-and-cone fracture mechanism as shown in Fig. 6d, which implies that the crack initiates at the centre forming a cup-shaped region, then grows outwards inclined and finally leads to the

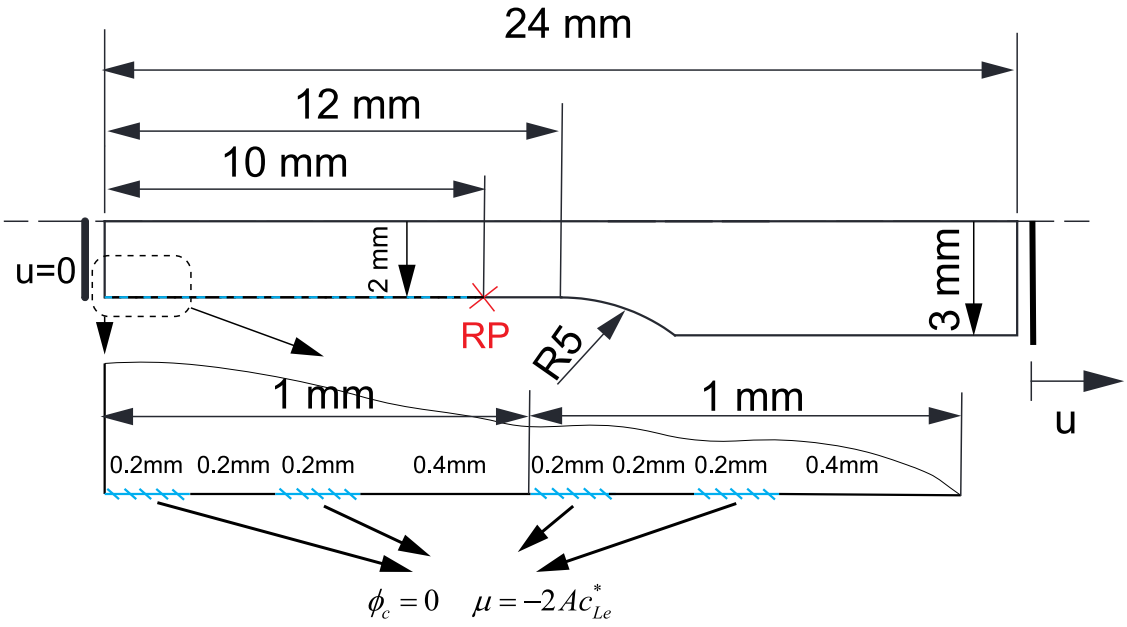

Fig. 5. Geometry and boundary conditions of the FEM model for the smooth round WE43 specimen.

Table 4
Parameters of the multiphase-field model calibrated for the WE43 alloy.

Parameter	Physical interpretation	Value
$\bar{H}$	Effective hardening modulus	770 MPa
$\bar{K}$	Effective bulk modulus	32173 MPa
$\bar{G}$	Effective shear constant	17480 MPa
$\bar{\sigma}_y$	Effective initial yield stress	260 MPa
l_d	Fracture interface thickness	0.1 mm (Gastaldi et al., 2011)
g_{dm0}	Initial critical fracture energy of WE43	85 MPa mm
$g_{dm\infty}$	Reduced critical fracture energy of WE43	$0.15g_{dm0}$ (Dittmann et al., 2018)
m_p	Plastic model parameter	5
γ_{crit}	Critical equivalent plastic strain	0.8
c_{solid}	Saturated Mg-ion concentration in WE43	67.319 mol/L (Shen et al., 2019)
c^*_{Le}	Normalised saturated Mg-ion concentration in the corroded material	0.051 (Shen et al., 2019)
g_c	Critical corrosion energy	0.01 N/mm
l_c	Corrosion interface thickness	0.1 mm (Gastaldi et al., 2011)
A	Free energy density curvature	53.5 N/mm^2
D_{cl}	Diffusion coefficient in electrolyte	8.5×10^{-4} mm^2/s (Lemkul and MacKerell, 2016; Höche, 2014)
D_{cp}	Diffusion coefficient in intact material	3.5×10^{-7} mm^2/s
L_c	Interface kinetics coefficient	2×10^{-2} mm^2/(Ns)
g_{dc}	Critical fracture energy of corrosion product	$0.01g_{dm}$
m_d	Fracture model parameter	2.4
m_c	Corrosion model parameter	3

cone-form fracture (Anderson, 2017). The final distribution of the crack phase-field and the evolution of the equivalent plastic strain near the damage zone are illustrated in Figs. 6b and 6c, respectively. It is shown that the model is able to reproduce the cup-and-cone fracture process of WE43 by considering the strong interaction between plastic deformation and fracture. The computational simulation of the fracture process demonstrates that microvoids represented by crack phase-field initially develop within the middle section of the specimen due to high stress triaxiality and plastic deformations, leading to crack nucleation. As a result of the formation of a large damage zone with further increase of loading, the material near the tip of the initial penny-shaped crack suffers a very high level of strain at about 45° relative to the plane of flat crack.

The model parameters related the critical fracture energy have significant impact on the fracture behaviour and thus need to be studied quantitatively. To this end, using the aforementioned smooth WE43MEO specimen, we will investigate the effect of material parameters g_{dm0}, m_p and γ_{crit}, which relate to the interaction between plastic deformation and fracture. Firstly, we demonstrate the influence of the initial critical fracture energy g_{dm0} on the damage behaviour, which is directly reflected on the force–displacement curves presented in Fig. 7a. It is show that an increase in g_{dm0} leads to a higher tensile strength and larger plastic deformations leading to the final failure of the specimen. Additionally, the plastic hardening is more apparent in the early stage of plastic deformations, due to higher damage resistance of larger g_{dm0}. As shown in Fig. 7b, g_{dm0} has limited effects on the crack path and damage pattern

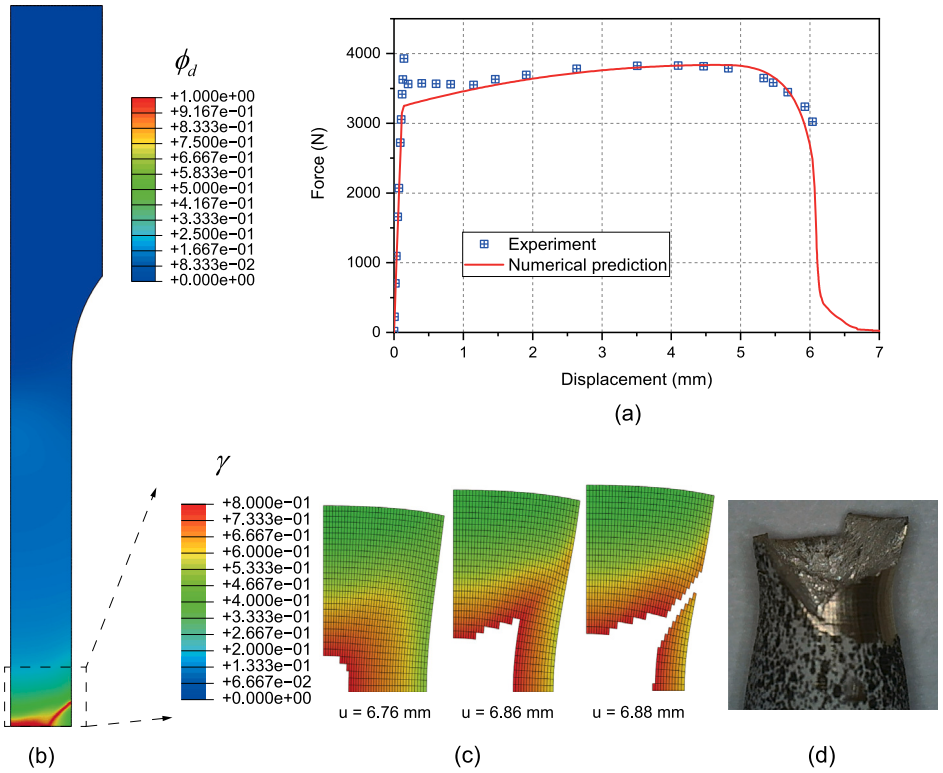

Fig. 6. Experimental and computational results of uniaxial tensile test: (a) force versus displacement curve, (b) distribution of crack phase-field after complete fracture, (c) evolution of equivalent plastic strain at various stages in the deformed configuration at u = 6.76, 6.86 and 6.88 mm and (d) fracture morphology observed in experiment.

under the premise of ductile fracture. Fig. 7a illustrated that the ultimate strength decreases from 322 MPa (corresponding tension force: 4050 N) to 288 MPa (corresponding tension force: 3617 N) in the case of g_{dm0} varying from 100 MPa mm to 70 MPa mm.

Figs. 8a and 8b compare the force–displacement curves predicted with different γ_{crit} and m_p, respectively, where g_{dm0} = 85MPa mm. It is evident that γ_{crit} affects the crack propagation rate. By increasing γ_{crit}, the necking leading to a large damage extension is progressively delayed. However, in contrast to the effect of g_{dm0}, γ_{crit} have less effects on the softening behaviour of material, as shown in Fig. 8a. In addition, there is almost no significant difference in the fracture strength in the case of $\gamma_{crit} > 0.7$. It is implied that a larger γ_{crit} results in a reduction of the crack propagation rate and affects the necking behaviour. As it can be seen from Fig. 9a, although γ_{crit} exhibits an invisible effect on the crack propagation path, it significantly affects the degree of damage and plastic deformations in the vicinity of the crack. The specimen with higher γ_{crit} undergoes more pronounced damage localisation, while a lower γ_{crit} causes more damage developed in the surrounding material. Therefore, an appropriate value for γ_{crit} is suggested to control the rate of crack propagation without changing the model's prediction on the crack path and the fracture strength.

The model parameter m_p governs the degradation rate of g_d with the equivalent plastic strain γ. An increase in m_p results in a sharper variation of g_d in the vicinity of γ_{crit} and converges to a step function, leading to delayed formation of the final crack and higher crack propagation rate, as demonstrated in Fig. 8b. Unlike the effect of γ_{crit} on the force–displacement curve, m_p can influence the softening behaviour of material prior to the formation of final crack. As shown in Fig. 8b, the maximal tension force of $m_p = 2$ is significantly lower than the other curves. Fig. 9b provides further insight into the influence of m_p on the fracture morphology, which shows that an increase in m_p enlarges the 'cup' region and reduces the 'cone' region. Therefore, the computational simulation with an appropriate value of m_p can predict different fracture patterns in addition to the global force–displacement characteristic.

5.2.2. Experimental and computational results of immersion tests

The corrosion model parameters are calibrated by comparing the degradation of the elastic modulus and the tensile ultimate strength of corroded specimens after 7, 14, 21 and 28 days, respectively. This is achieved by setting up two analysis steps in Abaqus. In the first step, only corrosion-related boundary conditions are defined for the specimen as shown in Fig. 5, while the second step involves only displacement boundary conditions. To account for the dissolution on the corrosion product and the post-immersion washing treatment, elements with a ϕ_c value below 0.1 are removed after completing the computation in the first corrosion step.

Fig. 10a shows the evolution of pits morphology after 7, 14, 21 and 28 days. It can be observed in the simulation that the pits begin to strongly interact with each other after 7 days. In the experiment, we observed a very distinct semi-elliptical pit merging

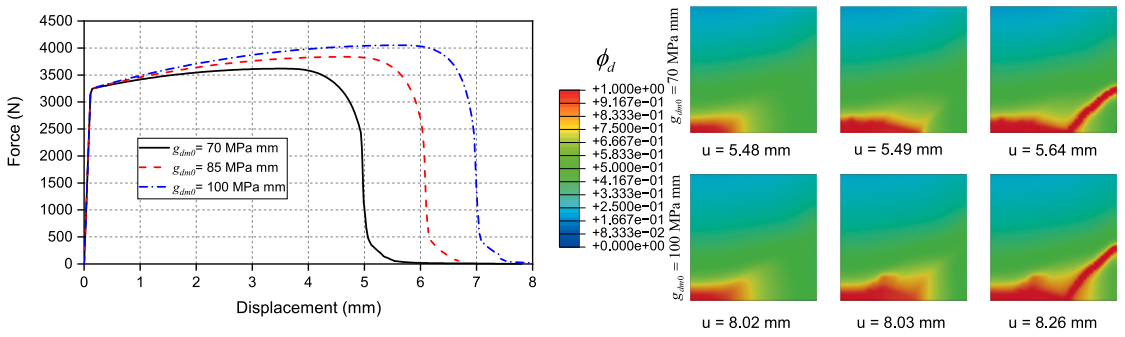

Fig. 7. Effect of the elastic critical fracture energy g_{dm0} on the fracture process. (a) Force versus displacement curves and (b) crack phase-field distribution near the final crack at various fracture stages at u = 5.48, 5.49, 5.64 mm for d_{dm0} = 70 MPa mm and u = 8.02, 8.03, 8.26 mm for d_{dm0} = 100 MPa mm.

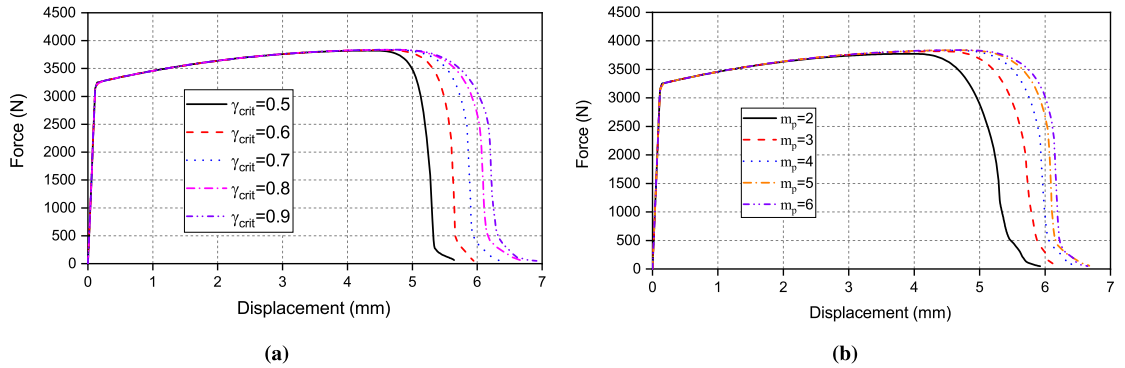

Fig. 8. Force versus displacement curves. (a) Effect of γ_{crit} on the fracture behaviour and (b) effect of m_p on the fracture process.

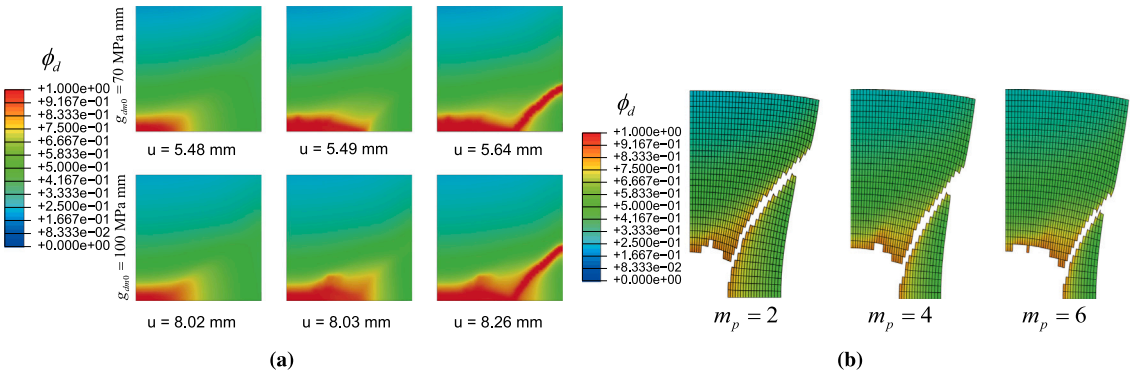

Fig. 9. Final fracture morphology on the deformed configuration under a residual loading of 50 N. (mid-section of the specimen as illustrated in Fig. 6) The elements with the value of $\phi_d > 0.9$ are removed. (a) Effect of γ_{crit} on the fracture process and (b) effect of m_p on the fracture process.

with neighbouring pit after 7 days as shown in Fig. 10c. As corrosion proceeds, pits in close proximity coalesce to form wider pits and continue to grow as shown in Fig. 10a similar to the pits we have observed in the immersion tests as shown in Fig. 10c, which are several hundred micrometres wide. Fig. 11 shows the degradation of the elastic modulus and the tensile ultimate strength after the corresponding immersion times. The predicted tensile strength decreased by 12.8% after 7days, 17.6% after 14 days, by 22.2% after 21 days, and by 25.0% after 28 days. The predicted degradation of the elastic modulus is almost identical to that of the tensile strength. It is implied that the stress concentration effect of pits is neglectable due to flat-shape of the pits. It is noteworthy that the mechanical properties decrease at a progressively slower rate after 7 days, which is consistent with the rate of corrosion. To

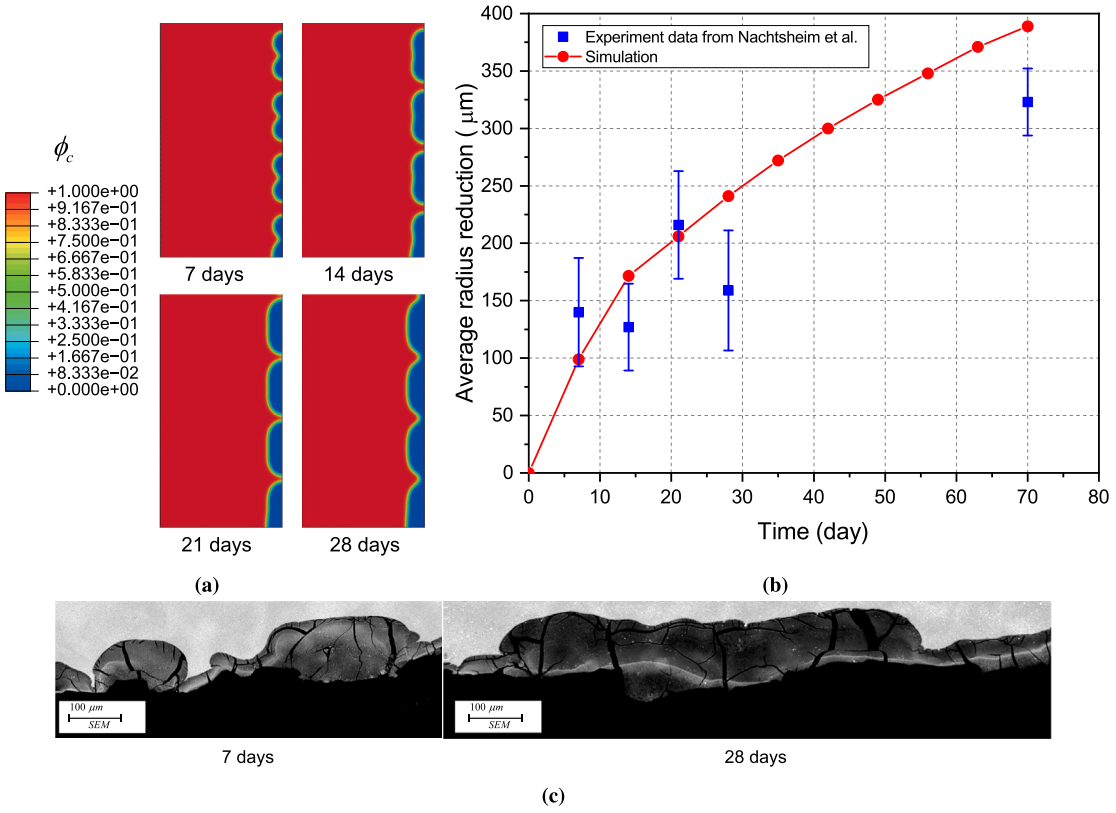

Fig. 10. Experimental and computational results of immersion tests. (a) Simulated evolution of corrosion morphology during a 28-day immersion test after 7, 14, 21 and 28 days, (b) average radius reduction versus time curve (Nachtsheim et al., 2022) and (c) SEM images of pits after 7-day and 28-day immersions.

quantitatively analyse the corrosion process, the reduction in average radius is calculated using

$$\Delta R = R_0 - \sqrt{\frac{V_{metal}}{\pi L_{middle}}}, \tag{99}$$

where R_0 is the initial radius, V_{metal} is the volume of intact material and L_{middle} is the length of specimen exposed to solution. In Fig. 10b, we compare the overall corrosion rates of the specimens from experiments and simulations rather than the depth of individual pits. The predicted average radius reduction of specimens agrees with the experimental data from Nachtsheim et al. in Nachtsheim et al. (2022). It is evident that the predicted average radius reduction reaches 100 μm after 7 days, 173 μm after 14 days, 205 μm after 21 days and 241 μm after 28 days, with a noticeable decrease in the growth rate over time. It is emphasised that the axisymmetric model leads to underestimating the maximum pit depth.

As the specimens corrode in DMEM with a longer immersion period, proteins continuously participate in the degradation process and can inhibit the corrosion process of magnesium alloys through adsorption and chelation in the corrosion layer (Wei and Gao, 2023). In addition, the alternation of ions in DMEM with increasing immersion time can slow down the corrosion rate (Wagener and Virtanen, 2016). Furthermore, at the microscopic level, there are micropores or cracks in the corrosion layer (Feliu and Llorente, 2015; Törne et al., 2017). These microdefects are gradually filled by insoluble precipitates or proteins over time, resulting in a decrease in the corrosion rate (Ascencio et al., 2014; Chen et al., 2020). These temporary evolutions of reaction and diffusion resistance of the corrosion system are not accounted for in the simulation. As a result, the corrosion rate for the immersion time of 70 days is overestimated in the simulation, compared to the experimental data.

It is generally accepted that the corrosion product layer in the DMEM medium with a controlled pH value is quite stable (Grogan et al., 2014). In our experiments, we observed that the stable corrosion layer covered the specimen surface in the immersion test and exhibited remarkable stability in DMEM with negligible dissolution, which is consistent with the experimental results in van Gaalen et al. (2023b). By analysing the corroded specimens, it was observed that the diameter of the specimens with the corrosion layer remained almost unchanged throughout the 70-day immersion test. The increase in the protectiveness of corrosion products of Mg alloys in DMEM over time was also reported in Cai et al. (2021). Consequently, this study does not account for the dissolution of the corrosion layer.

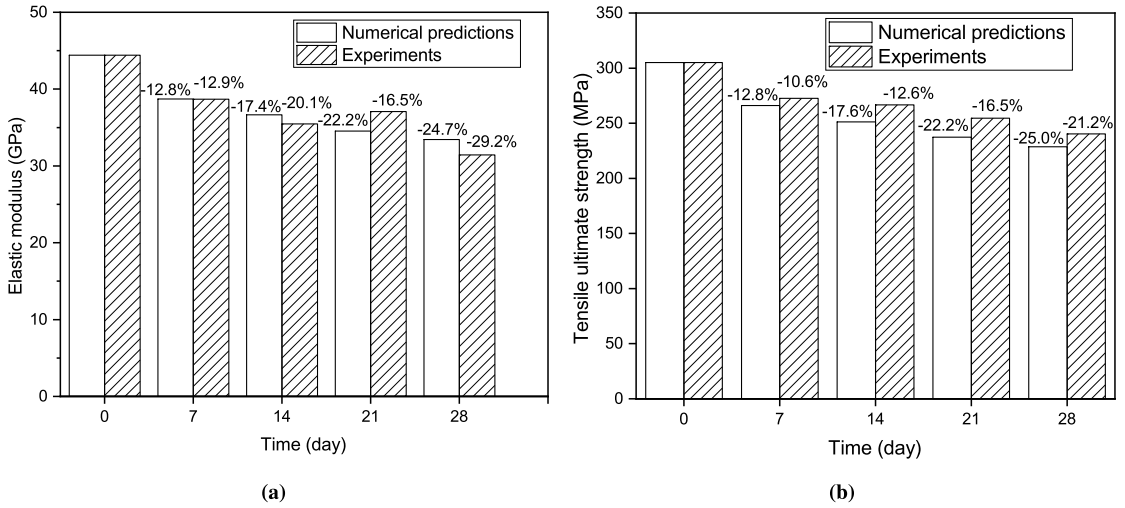

Fig. 11. Immersion tests. Tensile test data of each specimen after specified immersion time: (a) residual elastic modulus and (b) residual tensile ultimate strength.

5.2.3. Experimental and computational results of SSRTC tests

In SSRTC tests, the fracture and corrosion processes are strongly coupled with each other under mechanical and electrochemical loadings. In addition, the corrosion product layer on the surface under high stresses suffer significant damage, leading to a higher corrosion rate of the substrate of magnesium alloy. In the present model, the interaction between fracture and corrosion is considered by varying the diffusion mobility with crack phase-field and the coupling terms in the dissipation potential. To validate the model for predicting the stress corrosion cracking behaviour, we carried out experiments and computational simulations of the SSRTC tests with 0.3 mm/h, 0.1 mm/h and 0.06 mm/h loading rates.

Fig. 14 shows that force–displacement curves of these SSRTC tests. It is seen that the fracture displacement under loading rates of 0.3 mm/h, 0.1 mm/h and 0.06 mm/h are 1.6 mm, 1.93 mm and 2.76 mm, respectively. The specimen subjected to a smaller loading rate experiences a longer corrosion time to failure. These results are in good agreement with the findings reported by Prabhu et al. (2018) regarding the relationship between strain rates and fracture stresses of biodegradable Mg alloy in simulated body fluids. This suggests that the specimen will fail in more brittle manner under sufficiently slow loading rates due to corrosion. In general, the computational results are in good agreement with experimental results. Fig. 15 shows the distribution evolution of the crack phase-field and corrosion phase-field in the midsection. The simulation results show that more significant pitting corrosion appears in the axial centre of the specimen after 22.6 h, where the damage process due to the stress concentration can significantly accelerate the corrosion process. In the initial stage of the SSRTC tests, only the corrosion products undergo fracture, which is reflected in Fig. 15 for t = 22.6 h and 26.0 h, where $\phi_d = 1$ is exclusively observed in regions with $\phi_c = 0$. Therefore, prior to the occurrence of fracture in the magnesium alloy substrate, the corrosion field ϕ_c and crack field ϕ_d consistently interact and follow each other. During the final fracture stage, as the load increases and localised pitting becomes more pronounced, the uncorroded material experiences significant plastic deformation due to stress concentrations. This leads to the rapid expansion of cracks into the alloy substrate. Consequently, the material in the vicinity of the final fracture zone does not have sufficient time to undergo complete corrosion.

The high degree of microstructural heterogeneity in the corrosion layer, *e.g.*, material heterogeneity, surface roughness, and microdefects (Naterer et al., 2006) can result in the initiation and propagation of microcracks (Feliu and Llorente, 2015; Törne et al., 2017) in the corrosion layer under increasing mechanical loadings. In the macroscale simulation, the microstructural heterogeneity was not considered, which leads to homogenous deformations and damage of the corrosion layer under uniaxial tensile conditions. The predicted high damage value of $\phi_d > 0.8$ in the whole corrosion product layer represents a high overall damage degree in the corrosion layer.

To computationally demonstrate the influence of the microstructure of the corrosion layer on crack propagation during the SSRTC test, we use a segment of the specimen with a height of 100 μm and a width of 1000 μm. The microdefects representing microstructural heterogeneity are introduced in the outer layer with a thickness of 20 μm, as illustrated in Fig. 12. The element size of the outer layer is 0.25 μm. The segment is subjected to uniaxial tension with a strain rate of 0.06 mm/h as in the SSRTC experiments, and the other boundary conditions are shown in Fig. 12. Four notches with a radius of 2.5 μm are uniformly distributed on the outer surface. The diameter of inner pores is randomly generated between 1.5 and 5 μm, and the total porosity is 0.05. The length scales of the phase field model are taken as 1 μm for the microscopic simulation. Adjustments of the critical fracture and corrosion energies ensure that the material maintains the same tensile strength and the imposed corrosion energy barrier, following (Kristensen et al., 2021; Abubakar et al., 2015). The other material parameters are identical to Table 4. This computational example is utilised to qualitatively study the stress corrosion cracking of the corrosion layer at the microscale. Fig. 13 shows the predicted crack pattern in the corrosion layer as corrosion advanced from the surface. It is clearly observed that the microdefects affect the crack propagation path as

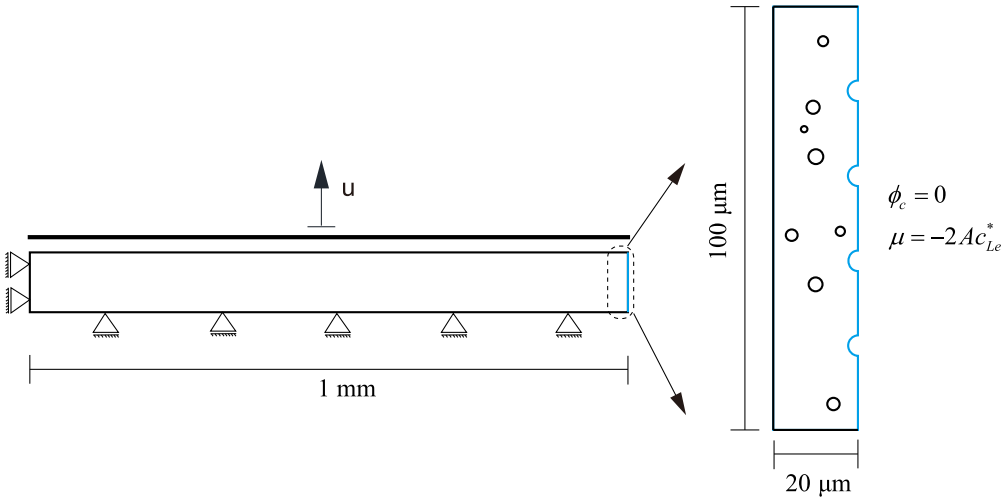

Fig. 12. Geometry and boundary conditions of the microscopic model with microstructural heterogeneity.

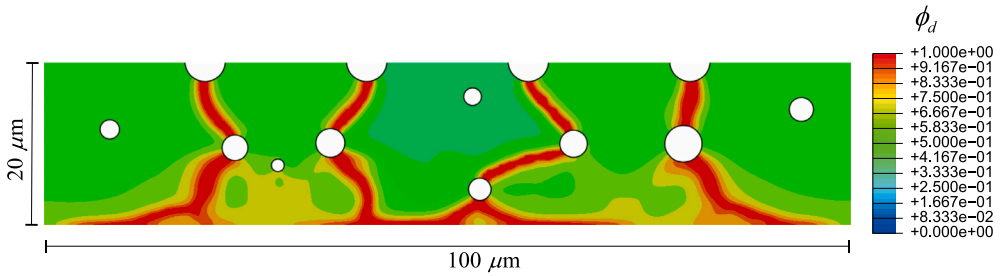

Fig. 13. Crack pattern of the corrosion layer with microdefects.

well as the delamination between the corrosion layer and the alloy substrate. As demonstrated in the computational simulation, the microcracks initiate at the surface defects, connect the larger micropores, and trigger final delamination at the interface as corrosion degrades the magnesium alloy. To include the high-fidelity simulation of crack propagation paths in the corrosion layer, high computational costs or multiscale modelling methods are necessary for considering the microstructural heterogeneity. The fracture field within the corrosion product layer of the macroscopic simulation only indicates the overall degree of damage or microcrack density in the corrosion layer and accelerates the corrosion process due to the coupling functions in the variationally consistent modelling framework.

5.3. Computational analysis of corrosion-fracture interactions in notched round bar

In order to study effects of m_c and m_d on the interaction of fracture and pitting corrosion processes, we perform computational simulations of a notched round bar with the diameter of 6 mm and the height of 4 mm, where only the notch with the radius of 0.5 mm is immersed in fluids. Due to the symmetry of the notched round bar, one-half axisymmetric model of the bar is used in the finite element simulations. The material properties are identical to those for WE43. The finite element model consists of 8-node fully integrated axisymmetric elements with a maximum mesh size of 0.03 mm in the region near the notch, where corrosion occurs. At the time $t = 0$, $\mu = 2Ac^*_{Le}$ and $\phi_c = 1$ are defined as initial conditions in the notched bar, while $\mu = 0$ and $\phi_c = 0$ always hold at the notch as boundary conditions illustrated in Fig. 16. The upper edge is loaded vertically at a constant slow loading rate 300 μm/day.

First, we evaluate the effect of the coupling function h_{dc} as defined in Eq. (32) on stress corrosion cracking by fixing the fracture model parameter $m_d = 2$ defined in Eq. (36). The corrosion model parameter m_c in the coupling function h_{dc} governs the degradation rate of the critical fracture energy across the corrosion interface and thereby affects the corrosion dissipation, as described in Eq. (30) and (44). The dependency of the critical fracture energy on the corrosion phase-field results in an additional energetic driving force for species dissolution. Fig. 17a shows the evolution of pit depth versus time for different values of m_c. As m_c increases, the stress corrosion cracking proceeds with a higher rate. The stable corrosion rate for $m_c = 2$ is 0.09 mm/h, and it increases to 0.11 mm/h for $m_c = 4$. However, the morphology of the corrosion interfaces shows no significant difference, as shown in Fig. 17b. SCC proceeds mainly in the radial direction, following the concentration of stress, where the corrosion product is more likely to fracture. On the other hand, the pit grows relatively slowly in the axial direction. We can observe a change in the morphology of the pits in Fig. 17b. Due to the complete fracture of the round bar, the fluid infiltrates the entire fractured region, forming a narrow pit.

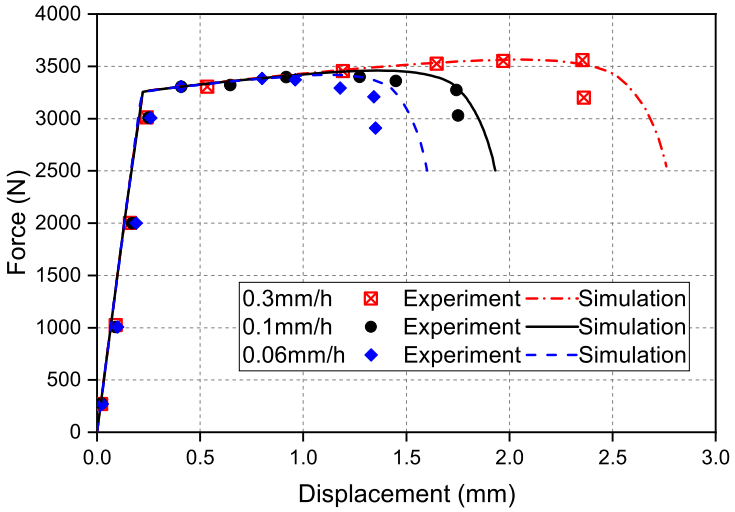

Fig. 14. Experimental and computational results of load–displacement curves under three loading rates in SSRTC tests.

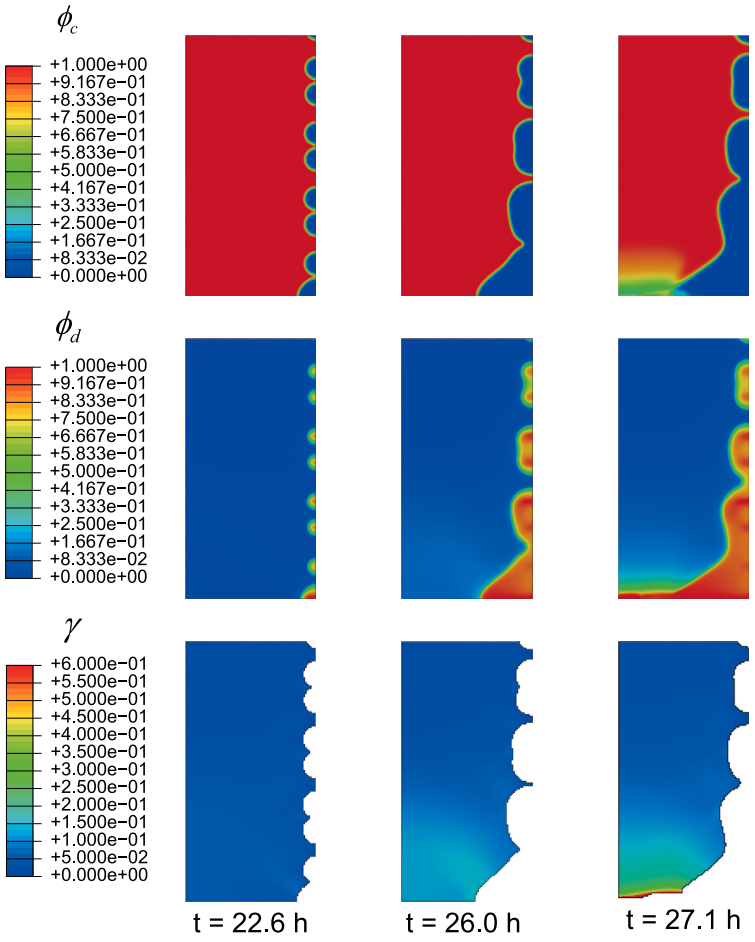

Fig. 15. Simulation results of SSRTC tests. The evolution process of corrosion morphology, distribution of crack phase-field and the equivalent plastic strain in the midsection under the loading rate $v = 0.06$ mm/h. Highly damaged elements ($\phi_c < 0.1$ and $\phi_d > 0.9$) are removed to illustrate the equivalent plastic strain γ.

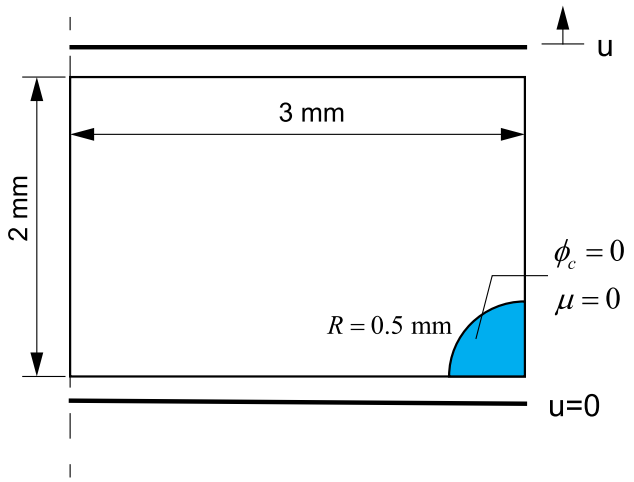

Fig. 16. Geometry and boundary conditions of notched round-bar.

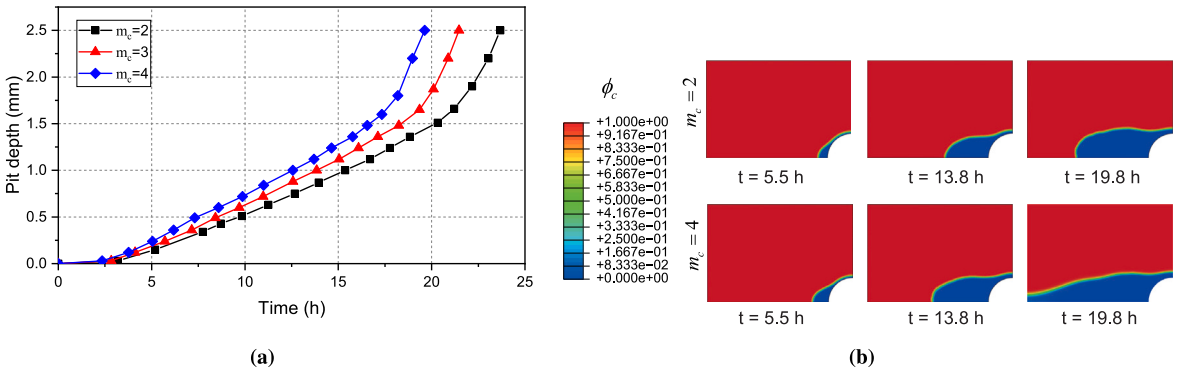

Fig. 17. Effect of m_c on the fracture process of the notched round-bar. (a) Pit depth-time curve and (b) corrosion interface morphology at t = 5.5 h, 13.8 h, 19.8 h.

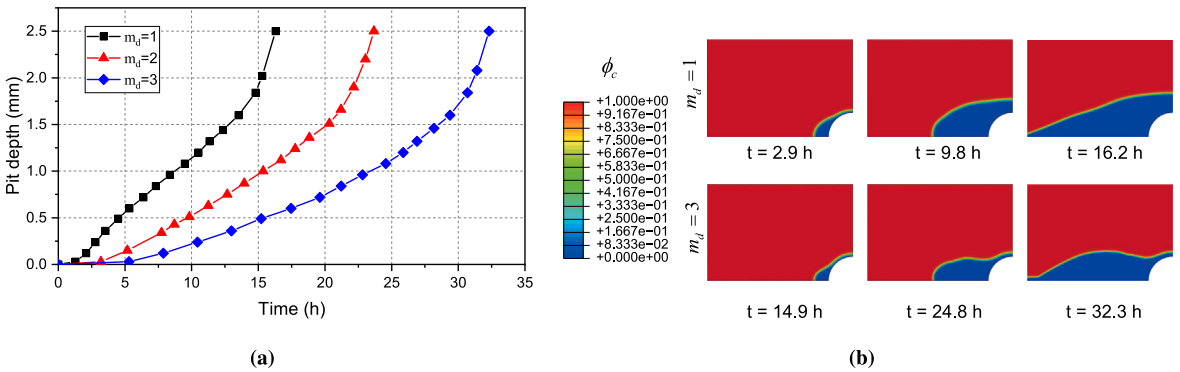

Fig. 18. Effect of m_d on the fracture process of the notched round-bar. (a) Pit depth-time curve and (b) corrosion interface morphology at t = 2.9 h, 9.8 h, 16.2 h for m_d=1 and t = 14.9 h, 24.8 h, 32.3 h for m_d= 3.

The presence of the corrosion product hinders the direct contact with electrolyte and reduce the migration rate of species, resulting in a lower corrosion rate. However, the external loading can easily damage its weak structure of the corrosion layer with much lower fracture resistance and generate micro or macrocracks in the corrosion product, providing a pathway for the electrolyte to penetrate. The coupling effect of corrosion product fracture on the diffusivity of ions is captured by the coupling function h_f as specified in Eq. (36) for considering the penetration capacity of the electrolyte into the material at different levels of damage. We exam the influence of the model parameter m_d in the function of h_f with a fixing corrosion model parameter $m_c = 2$. Figs. 18a

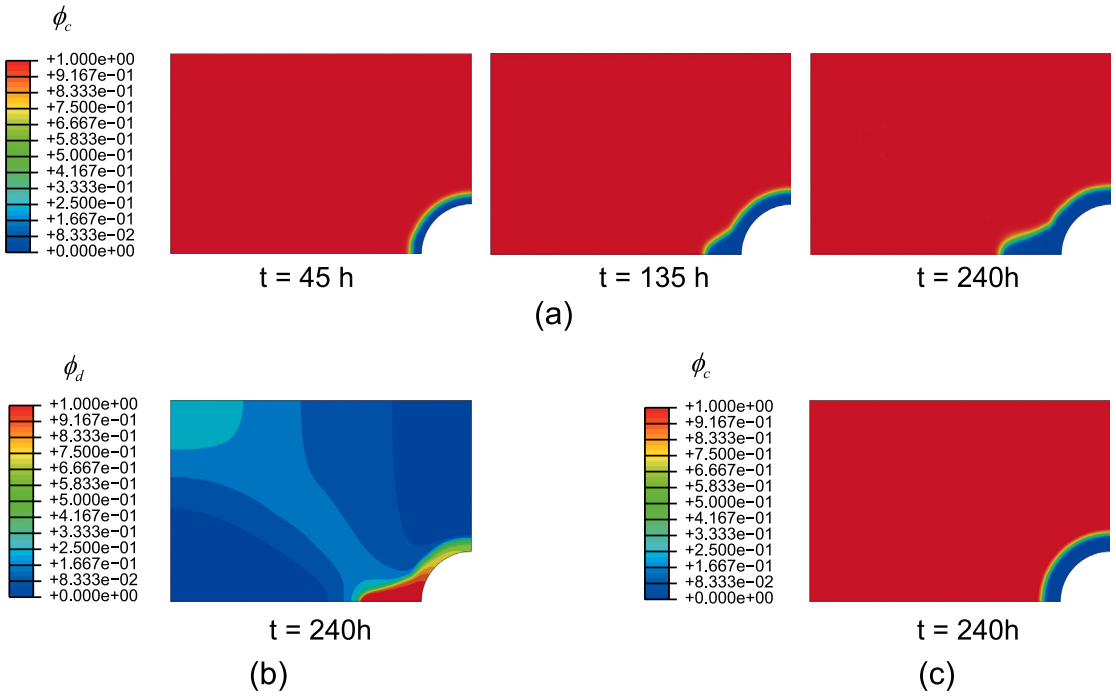

Fig. 19. Contribution of the coupling term $\mathfrak{D}^{dc}$ to the corrosion process. (a) corrosion morphology at t = 45 h, 135 h and 240 h, (b) crack phase field distribution at t = 240 h and (c) corrosion morphology at t = 240 h by neglecting $\mathfrak{D}^{dc}$ in the model.

and 18b show effects of m_d on the corrosion process in terms of pit depth and corrosion morphology respectively. The average pit growth rate is 0.15 mm/h at $m_d = 1$ and reduces to 0.077 mm/h at $m_d = 3$. As depicted, a higher m_d leads to a slower corrosion process more apparently in regions with high stress concentrations. A high value of m_d implies that the electrolyte can only infiltrate the material effectively after complete fracture.

Furthermore, to demonstrate the influence of the corrosion-fracture coupling term $\mathfrak{D}^{dc}$, we eliminate the variation in diffusion coefficient by setting the diffusion coefficient D_c to a constant value 3.5×10^{-7} mm^2/s independent from the crack field ϕ_d and L_c to be 2×10^{-5}mm^2/(Ns). The upper boundary is tracked at a constant velocity $v = 40$ μm/day. In the early stages of the simulation, when the displacement is small, corrosion occurs almost uniformly in all directions at t = 45 h (Fig. 19(a)). As the localised damage become larger (Fig. 19(b)), the corrosion morphology distinctly transits to pit after 135 h. To provide a basis for comparison, Fig. 19(c) presents the computational results obtained in the absence of the coupling term $\mathfrak{D}^{dc}$. It indicates that external loads directly contribute to the corrosionl rate. For more accurate modelling of pit-to-crack transition, an additional coupling between corrosion and mechanical deformations proposed in Cui et al. (2022) can be used.

6. Conclusions

In this work, we have proposed a multiphase-field model for modelling ductile fracture and pitting corrosion in biodegradable magnesium alloys based on a variational framework. Three coupling functions, representing the degradation of mechanical properties by fracture, reduction of critical fracture energy by corrosion and the enhancement of ion diffusion mobility by fracture, are utilised and naturally integrated within a thermodynamically consistent framework for capturing the interactions between fracture field and corrosion morphology. We have derived the FEM formulations based on the time-discrete incremental variational principle and implemented in the staggered scheme through a 2-layer-element structure in Abaqus. The feasibility of the proposed model is validated through in vitro experiments with tensile specimens of bioabsorbable magnesium rare-earth alloy WE43MEO, previously detailed in (Nachtsheim et al., 2022, 2024). The experimental and computational results provide insights into the crack propagation process, evolution of pits and interactions between mechanical and chemical damages. Furthermore, we have conducted a numerical study on the model parameters of the coupling functions to understand their impact on the material degradation behaviours. Based on the experimental and computational results, the following conclusions can be drawn:

- The present phase-field model can capture the experimentally observed inelastic deformation, necking and cup-and-cone fracture behaviours of magnesium alloy WE43MEO. Moreover, the material parameters in the coupling function between the critical fracture energy and the accumulated plastic strain enable a more accurate prediction of the softening behaviour after necking.

- The experimental and computational results of immersion tests reveal that the long-term in vitro corrosion of magnesium alloy WE43MEO in the cell culture medium is dominated by the diffusion-controlled process with a decreased corrosion rate. It is indicated that the corrosion products adhering to the surface of the magnesium alloy can effectively inhibit the reaction between magnesium alloys and the electrolyte. The predicted growth and fusion of pits during the corrosion process reasonably reflect the evolution of pit morphology under in vitro conditions.
- The stress corrosion experiments with different loading rates confirm that mechanical loading has a significant influence on the corrosion process. Lower loading rates lead to higher corrosion damage and significantly smaller fracture strains of biodegradable magnesium alloys in corrosive environments. Fracture of corrosion products due to high stresses results in a higher corrosion rate of the substrate of magnesium alloys, which can be predicted by utilising the coupling functions h_{dc} and h_f for modelling the interaction between the fracture and corrosion processes. However, the proposed model overestimates the fracture displacement in comparison with in vitro experiments, which can be attributed to the neglect of hydrogen embrittlement effects on the alloy matrix. The hydrogen embrittlement of magnesium alloys in simulated body fluid environments under mechanical loadings has been observed in AZ91D Mg alloys by Jafari et al. (2015c) and in WE43 by Choudhary et al. (2014). The modelling approach proposed in Cui et al. (2022) can be utilised to extend the present multiphase-field model for considering the hydrogen embrittlement of magnesium alloys. More detailed in vitro experimental investigation on hydrogen embrittlement of magnesium alloys under mechanical loadings are required in the future work for modelling stress corrosion cracking of magnesium alloys.
- The reasonable agreement between experimental results and computational predictions demonstrates the ability of the proposed multiphase-field model for accurately predicting the material response of biodegradable magnesium alloys under chemo-mechanical loading conditions, which plays an important role in in silico design and the assessment of the mechanical integrity of biodegradable magnesium implants in physiological environments.

The present study focuses on the long-term corrosion behaviour of bioabsorbable magnesium alloys and thereby neglected detailed electrochemical mechanisms of activation-controlled corrosion. Considering magnesium ions as charged particles and integrating the effects of electrochemistry can improve the general predictive ability of the present model for activation-controlled corrosion. As mentioned in Section 2.1, the complex electrochemical reactions among ions during the corrosion process are not accounted for in the current model. Consequently, this leads to a lack of physical modelling of the corrosion product growth and dissolution processes. Additionally, the driving effects of electric potential on electrochemical reactions and ion diffusion are not considered. These limitations could be addressed in future research by physically based modelling of the transport of charged species, the electric potential distribution, and corrosion products formation/dissolution.

CRediT authorship contribution statement

Dawei Zhang: Writing – original draft, Methodology, Investigation, Data curation, Conceptualization. **Songyun Ma:** Writing – review & editing, Supervision, Project administration, Methodology, Funding acquisition, Conceptualization. **Julia Nachtsheim:** Writing – review & editing, Methodology, Investigation, Conceptualization. **Shunqi Zhang:** Writing – review & editing, Methodology. **Bernd Markert:** Writing – review & editing, Supervision.

Declaration of competing interest

The authors declare that they have no known competing financial interests or personal relationships that could have appeared to influence the work reported in this paper.

Data availability

Data will be made available on request.

Acknowledgements

This research was supported by the Federal Ministry of Education and Research of Germany in the framework of RePlaSys (project number FKZ 13GW0352B), and the China Scholarship Council (CSC) (Reference No. 202108080318). The authors would like to thank Medical Magnesium GmbH and Meotec GmbH for supplying the alloy as well as Uwe Navrath, Mario Hackbarth and Thomas Derra for assisting the corrosion experiments.

Appendix A. Chemical bulk free energy

Following the KKS model (Kim et al., 1999), the ion concentration c^* and the chemical bulk free energy ψ_{bulk}^{ch} for a mixture of the two phases with different chemical compositions are approximated by

$$c^* = h_c(\phi_c)\, c_S^* + [1 - h_c(\phi_c)]\, c_L^*, \tag{100}$$

$$\psi_{bulk}^{ch} = h_c(\phi_c)\psi_S^{ch}(c_S^*) + [1 - h_c(\phi_c)]\psi_L^{ch}(c_L^*). \tag{101}$$

Here c_S^* and c_L^* are the normalised concentration of the coexisting metal phase and corrosion phase at a material point, respectively, while $\psi_S^{ch}(c_S^*)$ and $\psi_L^{ch}(c_L^*)$ are the corresponding local electrochemical energy density of each phase. $h_c(\phi_c)$ is a continuous interpolation function such that $h_c(\phi_c = 0) = 0$ and $h_c(\phi_c = 1) = 1$. In this study, a cubic function $h_c(\phi_c) = -2{\phi_c}^3 + 3{\phi_c}^2$ is used following (Mai et al., 2016). Furthermore, the chemical free energy density of each phase (Hu et al., 2007) can be expressed as

$$\begin{aligned} \psi_S^{ch}(c_S^*) &= A_S\,(c_S^* - c_{Se}^*)^2, \\ \psi_L^{ch}(c_L^*) &= A_L\,(c_L^* - c_{Le}^*)^2, \end{aligned} \tag{102}$$

where A_S and A_L are the free energy density curvature of metal phase and corrosion phase, respectively, and are determined according to thermodynamic database (Abubakar et al., 2015). c_{Se}^* and c_{Le}^* are the normalised equilibrium concentration in the metal matrix and the corroded phase, respectively. The KKS model (Kim et al., 1999) assumes that two phases of the mixture in dilute solutions has different concentrations but the identical chemical potential in a chemical equilibrium state, which is mathematically expressed as:

$$\frac{\partial \psi_S^{ch}(c_S^*)}{\partial c_S^*} = \frac{\partial \psi_L^{ch}(c_L^*)}{\partial c_L^*}. \tag{103}$$

Using Eqs. (100) and (103) to substitute c_S^* and c_L^* with c^* and ϕ_c, Eq. (101) for the chemical bulk free energy density can be recast as

$$\begin{aligned} \psi_{bulk}^{ch}(c^*, \phi_c) =& h_c A_S \left[\frac{A_L c^* + \left(1 - h_c\right)\left(A_S c_{Se}^* - A_L c_{Le}^*\right)}{h_c\left(A_L - A_S\right) + A_S} - c_{Se}^* \right]^2 \\ &+ (1 - h_c) A_L \left[\frac{A_S c^* + h_c\left(A_L c_{Le}^* - A_S c_{Se}^*\right)}{h_c\left(A_L - A_S\right) + A_S} - c_{Le}^* \right]^2. \end{aligned} \tag{104}$$

Assuming $A_S = A_L = A$ for both metal phase and corroded phases (Mai et al., 2016; Nguyen et al., 2018; Kovacevic et al., 2023), the chemical bulk free energy is simplified to

$$\psi_{bulk}^{ch}(c^*, \phi_c) = A\left[c^* - \left(1 - h_c(\phi_c)\right) c_{Le}^* - h_c(\phi_c) c_{Se}^*\right]^2. \tag{105}$$

Appendix B. Dissipation inequality

Letting $\mathfrak{e}$ and $\mathfrak{s}$ denoting the internal energy and entropy density per unit mass respectively, the energy balance and entropy inequality read

$$\frac{d}{dt}\int_\Omega \rho_0 \mathfrak{e}\, dV = \int_\Omega \mathbf{b}\cdot\dot{\mathbf{u}}\, dV + \int_{\partial\Omega} \left(\boldsymbol{t}\cdot\dot{\mathbf{u}} + \boldsymbol{t}_c\cdot\boldsymbol{n}\dot{c}^* - \mathfrak{e}^f \boldsymbol{h}\cdot\boldsymbol{n}\right) dA - \int_{\partial\Omega} \boldsymbol{q}\cdot\boldsymbol{n}\, dA + \int_\Omega \rho_0 r\, dV, \tag{106}$$

$$\frac{d}{dt}\int_\Omega \rho_0 \mathfrak{s}\, dV \geq -\int_{\partial\Omega} \mathfrak{s}^f \boldsymbol{h}\cdot\boldsymbol{n}\, dA - \int_{\partial\Omega} \frac{\boldsymbol{q}\cdot\boldsymbol{n}}{\Theta}\, dA + \int_\Omega \frac{\rho_0 r}{\Theta}\, dV, \tag{107}$$

where $\boldsymbol{q}$ is the heat flux, r is a heat source and Θ is absolute temperature. $\mathfrak{e}^f$ and $\mathfrak{s}^f$ denote the enthalpy and the specific entropy changes provided by a unit supply of specie flux. $\mathfrak{e}^f$ is equal to the pressure work plus the internal energy of the specie flux. Specifically, the pressure work is neglected in this study. The internal energy is written in terms of the Helmholtz free energy and entropy under the Legendre transformation as

$$\rho_0 \mathfrak{e} = \psi + \Theta \rho_0 \mathfrak{s}. \tag{108}$$

Using Eqs. (106) and (108), the entropy density $\mathfrak{s}$ in Eq. (107) can be substituted by the internal energy density $\mathfrak{e}$ and the free energy density ψ. In addition, we define the chemical potential of specie as

$$\mu = \mathfrak{e}^f - \Theta \mathfrak{s}^f. \tag{109}$$

As a result, the dissipation inequality leads to the global dissipation postulation for isothermal processes with $r = 0$, $\nabla\cdot\boldsymbol{q} = 0$ and $\nabla\Theta = 0$

$$D = \int_\Omega \mathbf{b}\cdot\dot{\mathbf{u}}\, dV + \int_{\partial\Omega} \left(\boldsymbol{t}\cdot\dot{\boldsymbol{u}} + \boldsymbol{t}_c\cdot\boldsymbol{n}\dot{c}^* - \mu\boldsymbol{h}\cdot\boldsymbol{n}\right) dA - \int_\Omega \dot{\psi}\, dV \geq 0, \tag{110}$$

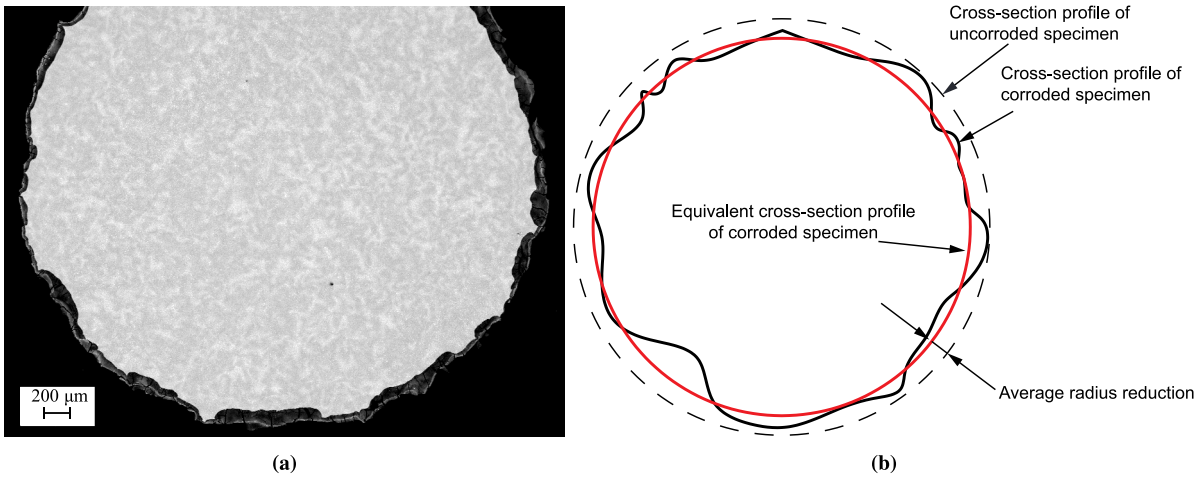

Fig. 20. (a) Cross-section SEM image of the corroded specimen after 28-day immersion test and (b) simplification of equivalent cross-section profile.

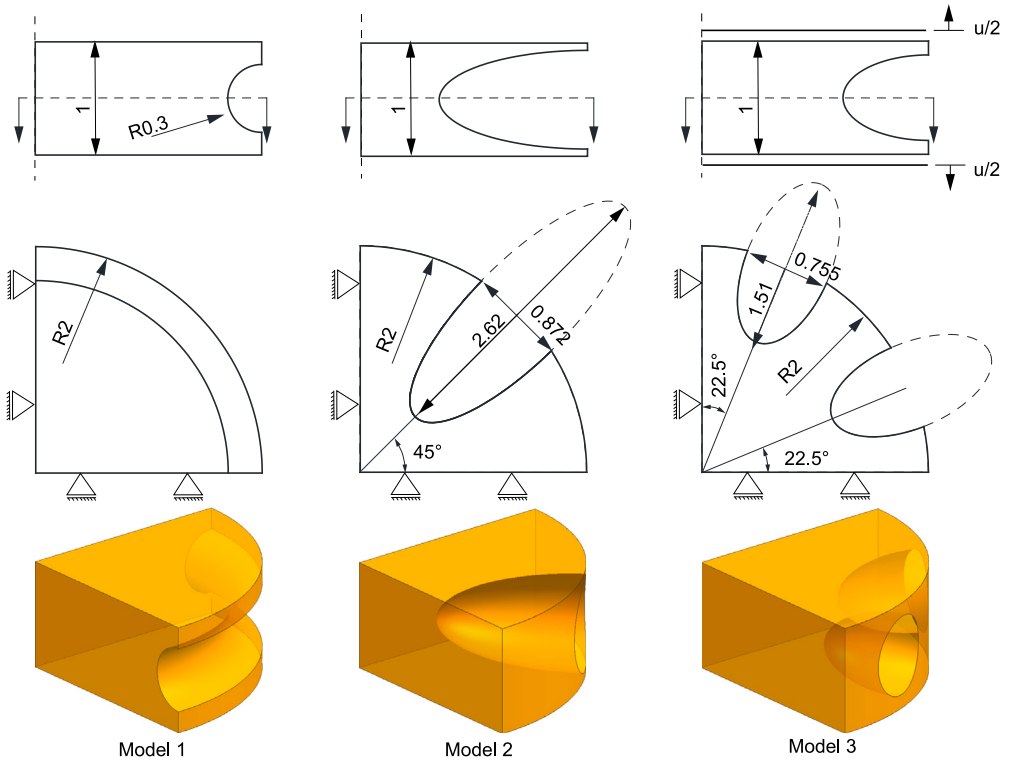

Fig. 21. Geometries and boundary conditions of models to study the difference between the axisymmetric model and 3D models with different pit depths (unit in mm).

Now, we substitute the rate of free energy density Eq. (21) into the dissipation inequality Eq. (110) and then obtain

$$
\begin{aligned}
D &= \int_{\Omega} \left(\boldsymbol{b} \cdot \dot{\boldsymbol{u}} - \boldsymbol{\sigma} : \dot{\boldsymbol{\varepsilon}} + \boldsymbol{\sigma} : \dot{\boldsymbol{\varepsilon}}^{p} - \sigma_{\gamma} \dot{\gamma} - \sigma_{f} \dot{\phi}_{d} - \sigma_{\phi_c} \dot{\phi}_{c} - \sigma_{c} \dot{c}^{*} \right) dV \\
&+ \int_{\partial\Omega} \left(\boldsymbol{t} \cdot \dot{\boldsymbol{u}} + \boldsymbol{t}_{c} \cdot \dot{c}^{*} - \partial_{\nabla c^{*}} \psi^{ch} \cdot \dot{c}^{*} - \mu \boldsymbol{h} \cdot \boldsymbol{n} \right) dA \\
&= \int_{\Omega} \left(\boldsymbol{\sigma} : \dot{\boldsymbol{\varepsilon}} - \boldsymbol{\sigma} : \dot{\boldsymbol{\varepsilon}}^{p} - \sigma_{\gamma} \dot{\gamma} - \sigma_{f} \dot{\phi}_{d} - \sigma_{\phi_c} \dot{\phi}_{c} - \mu \nabla \cdot M_{c} \nabla \mu \right) dV + \int_{\partial\Omega} -\mu \boldsymbol{h} \cdot \boldsymbol{n} \, dA \\
&= \int_{\Omega} \left(\sigma_{y} \dot{\gamma} - h_{d}'(\psi) \bar{\psi}^{ep+} \dot{\phi}_{d} - \sigma_{\phi_c} \dot{\phi}_{c} + M_{c} \nabla \mu \cdot \nabla \mu \right) dV \geq 0,
\end{aligned}
\tag{111}
$$

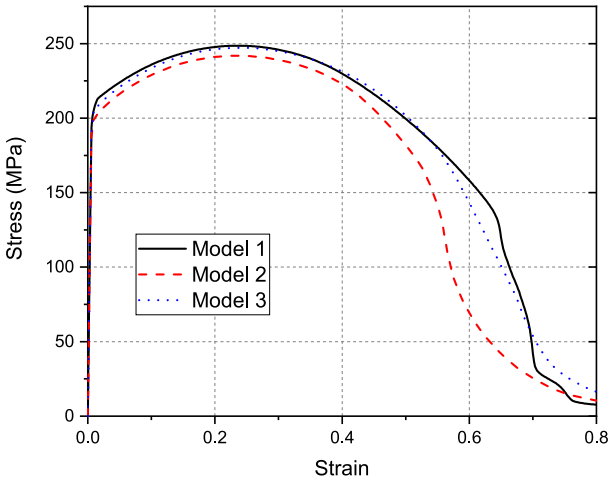

Fig. 22. Global stress–strain curves of the axisymmetric model and 3D models with different pit depths.

which results in the following statements: (1) the first term is nonnegative for $\sigma_y > 0$ and $\dot{\gamma} \geq 0$; (2) the second term is nonnegative since $-\sigma_f \geq 0$ and $\dot{\phi}_d \geq 0$; (3) the third term is nonnegative as $-\sigma_{\phi_c} \leq 0$ and $\dot{\phi}_c \leq 0$; and (4) the last term is nonnegative because of the quadratic function and $M_c > 0$.

Appendix C. Comparison between axisymmetric and 3D models

Fig. 20(a) shows the corroded cross-section of the specimen. It is observed that the inhomogeneous corrosion pits with moderate pit depths are distributed on the whole surface of the corrosion section in the circumferential direction. Due to the very high computational cost for the 3D simulation, we employed an axisymmetric model to compare the radius reduction of the equivalent corrosion profile from experiments and simulations, as illustrated in Fig. 20(b). The equivalent corrosion profile has an identical cross-section area to the real corrosion profile. The radius reduction of the equivalent corrosion profile reflects the overall corrosion rate of the whole specimen. We evaluated the computational difference between the axisymmetric model and two 3D models with different pit depths, as shown in Fig. 21. Model 1 features a semi-circular notch and can be simplified by an axisymmetric model. Model 2 incorporates an elliptical deep pit, and Model 3 consists of two elliptical shallow pits. All three models are designed with the same cross-sectional area in the middle of the model. The computed global stress and strain curves for the three models under uniaxial tension conditions are shown in Fig. 22. It is seen that the differences in the global stress–strain curves between Model 1 and Model 3 are only apparent in the last softening stage. However, the result of Model 2 with a deeper pit exhibits a slightly larger difference. The differences in the elastic modulus and the tensile strength extracted from the global stress–strain curves between Models 1 and 2 are less than 1%. Therefore, considering the observed moderate pit depth in the experiments, we employed the axisymmetric model to predict the reduction of the elastic modulus and the tensile strength of corroded specimens. Especially, the computational workload for the 3D simulation of slow strain rate tensile tests, where the fracture and corrosion are strongly coupled, is exceedingly high with the current computing infrastructure.

References

Abubakar, Abba Abdulhamid, Akhtar, Syed Sohail, Arif, Abul Fazal M., 2015. Phase field modeling of V2o5 hot corrosion kinetics in thermal barrier coatings. Comput. Mater. Sci. 99, 105–116.

Ahmadi, Masoud, 2020. A hybrid phase field model for fracture induced by lithium diffusion in electrode particles of li-ion batteries. Comput. Mater. Sci. 184, 109879.

Alessi, Roberto, Marigo, Jean-Jacques, Maurini, Corrado, Vidoli, Stefano, 2018. Coupling damage and plasticity for a phase-field regularisation of brittle, cohesive and ductile fracture: one-dimensional examples. Int. J. Mech. Sci. 149, 559–576.

Amor, Hanen, Marigo, Jean-Jacques, Maurini, Corrado, 2009. Regularized formulation of the variational brittle fracture with unilateral contact: Numerical experiments. J. Mech. Phys. Solids 57 (8), 1209–1229.

Anderson, Ted L., 2017. Fracture Mechanics: Fundamentals and Applications. CRC Press.

Ascencio, M., Pekguleryuz, M., Omanovic, S.J.C.S., 2014. An investigation of the corrosion mechanisms of WE43 Mg alloy in a modified simulated body fluid solution: The influence of immersion time. Corros. Sci. 87, 489–503.

Barzegari, Mojtaba, Mei, Di, Lamaka, Sviatlana V., Geris, Liesbet, 2021. Computational modeling of degradation process of biodegradable magnesium biomaterials. Corros. Sci. 190, 109674.

Borden, Michael J., Hughes, Thomas J.R., Landis, Chad M., Anvari, Amin, Lee, Isaac J., 2016. A phase-field formulation for fracture in ductile materials: Finite deformation balance law derivation, plastic degradation, and stress triaxiality effects. Comput. Methods Appl. Mech. Engrg. 312, 130–166.

Bourdin, Blaise, Francfort, Gilles A., Marigo, Jean-Jacques, 2000. Numerical experiments in revisited brittle fracture. J. Mech. Phys. Solids 48 (4), 797–826.

Cahn, John W., Hilliard, John E., 1958. Free energy of a nonuniform system. I. Interfacial free energy. J. Chem. Phys. 28 (2), 258–267.

Cai, Changhong, Alves, Marta M., Song, Renbo, Wang, Yongjin, Li, Jingyuan, Montemor, M. Fátima, 2021. Non-destructive corrosion study on a magnesium alloy with mechanical properties tailored for biodegradable cardiovascular stent applications. J. Mater. Sci. Technol. 66, 128–138.
Chakraborty Banerjee, Parama, Al-Saadi, Saad, Choudhary, Lokesh, Harandi, Shervin Eslami, Singh, Raman, 2019. Magnesium implants: Prospects and challenges. Materials (Basel, Switzerland) 12 (1).
Chen, Lianxi, Blawert, Carsten, Yang, Junjie, Hou, Ruiqing, Wang, Xiaojian, Zheludkevich, Mikhail L., Li, Wei, 2020. The stress corrosion cracking behaviour of biomedical Mg-1Zn alloy in synthetic or natural biological media. Corros. Sci. 175, 108876.
Chen, Hong, Chang, Guixiang, Hao, Jianmin, 2024. Stress corrosion crack propagation behaviour of MAO ceramic coating on Mg alloy. Corros. Eng. Sci. Technol. 1478422X241236031.
Chen, Ziguang, Jafarzadeh, Siavash, Zhao, Jiangming, Bobaru, Florin, 2021. A coupled mechano-chemical peridynamic model for pit-to-crack transition in stress-corrosion cracking. J. Mech. Phys. Solids 146, 104203.
Choudhary, Lokesh, Raman, R.K. Singh, 2012. Magnesium alloys as body implants: fracture mechanism under dynamic and static loadings in a physiological environment. Acta Biomater. 8 (2), 916–923.
Choudhary, Lokesh, Raman, R.K. Singh, 2013. Mechanical integrity of magnesium alloys in a physiological environment: Slow strain rate testing based study. Eng. Fract. Mech. 103, 94–102.
Choudhary, Lokesh, Raman, R.K. Singh, Hofstetter, Joelle, Uggowitzer, Peter J., 2014. In-vitro characterization of stress corrosion cracking of aluminium-free magnesium alloys for temporary bio-implant applications. Mater. Sci. Eng. C 42, 629–636.
Cui, Chuanjie, Ma, Rujin, Martínez-Pañeda, Emilio, 2021. A phase field formulation for dissolution-driven stress corrosion cracking. J. Mech. Phys. Solids 147, 104254.
Cui, Chuanjie, Ma, Rujin, Martínez-Pañeda, Emilio, 2022. A generalised, multi-phase-field theory for dissolution-driven stress corrosion cracking and hydrogen embrittlement. J. Mech. Phys. Solids 166, 104951.
De Meo, Dennj, Diyaroglu, Cagan, Zhu, Ning, Oterkus, Erkan, Siddiq, M. Amir, 2016. Modelling of stress-corrosion cracking by using peridynamics. Int. J. Hydrog. Energy 41 (15), 6593–6609.
Dittmann, M., Aldakheel, F., Schulte, J., Wriggers, P., Hesch, 2018. Variational phase-field formulation of non-linear ductile fracture. Comput. Methods Appl. Mech. Engrg. 342, 71–94.
Dubey, Anshu, Jaiswal, Satish, Lahiri, Debrupa, 2019. Mechanical integrity of biodegradable Mg–HA composite during in vitro exposure. J. Mater. Eng. Perform. 28, 800–809.
Duda, Fernando P., Ciarbonetti, Angel, Toro, Sebastian, Huespe, Alfredo Edmundo, 2018. A phase-field model for solute-assisted brittle fracture in elastic-plastic solids. Int. J. Plast. 102, 16–40.
Esmaily, M., Svensson, J.E., Fajardo, S., Birbilis, N., Frankel, G.S., Virtanen, S., Arrabal, R., Thomas, S., Johansson, L.G., 2017. Fundamentals and advances in magnesium alloy corrosion. Prog. Mater. Sci. 89, 92–193.
Feliu, Jr., S., Llorente, Irene, 2015. Corrosion product layers on magnesium alloys AZ31 and AZ61: Surface chemistry and protective ability. Appl. Surf. Sci. 347, 736–746.
Francfort, Gilles A., Marigo, J.-J., 1998. Revisiting brittle fracture as an energy minimization problem. J. Mech. Phys. Solids 46 (8), 1319–1342.
van Gaalen, Kerstin, Quinn, Conall, Benn, Felix, McHugh, Peter E., Kopp, Alexander, Vaughan, Ted J., 2023a. Linking the effect of localised pitting corrosion with mechanical integrity of a rare earth magnesium alloy for implant use. Bioactive Mater. 21, 32–43.
van Gaalen, Kerstin, Quinn, Conall, Weiler, Marek, Gremse, Felix, Benn, Felix, McHugh, Peter E., Vaughan, Ted J., Kopp, Alexander, 2023b. Predicting localised corrosion and mechanical performance of a PEO surface modified rare earth magnesium alloy for implant use through in-silico modelling. Bioactive Mater. 26, 437–451.
Gao, Yuanming, Wang, Lizhen, Li, Linhao, Gu, Xuenan, Zhang, Kuo, Xia, Jie, Fan, Yubo, 2019. Effect of stress on corrosion of high-purity magnesium in vitro and in vivo. Acta Biomater. 83, 477–486.
Gastaldi, Dario, Sassi, V., Petrini, Lorenza, Vedani, Maurizio, Trasatti, S., Migliavacca, Francesco, 2011. Continuum damage model for bioresorbable magnesium alloy devices—Application to coronary stents. J. Mech. Behav. Biomed. Mater. 4 (3), 352–365.
Grogan, James A., Leen, Sean B., McHugh, Peter E., 2014. A physical corrosion model for bioabsorbable metal stents. Acta Biomater. 10 (5), 2313–2322.
Grogan, J.A., O'brien, B.J., Leen, S.B., McHugh, P.E., 2011. A corrosion model for bioabsorbable metallic stents. Acta Biomater. 7 (9), 3523–3533.
Gutman, E.M., 2007. An inconsistency in "film rupture model" of stress corrosion cracking. Corros. Sci. 49 (5), 2289–2302.
Hänzi, Anja C., Gerber, Isabel, Schinhammer, Michael, Löffler, Jörg F., Uggowitzer, Peter J., 2010. On the in vitro and in vivo degradation performance and biological response of new biodegradable Mg-Y-Zn alloys. Acta Biomater. 6 (5), 1824–1833.
Hermann, Alexander, Shojaei, Arman, Steglich, Dirk, Höche, Daniel, Zeller-Plumhoff, Berit, Cyron, Christian J., 2022. Combining peridynamic and finite element simulations to capture the corrosion of degradable bone implants and to predict their residual strength. Int. J. Mech. Sci. 220, 107143.
Höche, Daniel, 2014. Simulation of corrosion product deposit layer growth on bare magnesium galvanically coupled to aluminum. J. Electrochem. Soc. 162 (1), C1.
Hofstetter, Joëlle, Martinelli, Elisabeth, Pogatscher, Stefan, Schmutz, Patrik, Povoden-Karadeniz, Erwin, Weinberg, Annelie M., Uggowitzer, Peter J., Löffler, Jörg F., 2015. Influence of trace impurities on the in vitro and in vivo degradation of biodegradable Mg–5Zn–0.3 Ca alloys. Acta Biomater. 23, 347–353.
Hornberger, Helga, Virtanen, Sannakaisa, Boccaccini, Aldo R., 2012. Biomedical coatings on magnesium alloys–a review. Acta Biomater. 8 (7), 2442–2455.
Hu, S.Y., Murray, J., Weiland, H., Liu, Z.K., Chen, L.Q., 2007. Thermodynamic description and growth kinetics of stoichiometric precipitates in the phase-field approach. CALPHAD 31 (2), 303–312.
Huang, Liying, Wang, Kuaishe, Wang, Wen, Yuan, Jie, Qiao, Ke, Yang, Tao, Peng, Pai, Li, Tianqi, 2018. Effects of grain size and texture on stress corrosion cracking of friction stir processed AZ80 magnesium alloy. Eng. Fail. Anal. 92, 392–404.
Isfandbod, Mehrdad, Martínez-Pañeda, Emilio, 2021. A mechanism-based multi-trap phase field model for hydrogen assisted fracture. Int. J. Plast. 144, 103044.
Jafari, Sajjad, Harandi, Shervin Eslami, Singh Raman, R.K., 2015a. A review of stress-corrosion cracking and corrosion fatigue of magnesium alloys for biodegradable implant applications. JOM 67 (5), 1143–1153.
Jafari, Sajjad, Harandi, Shervin Eslami, Singh Raman, R.K., 2015b. A review of stress-corrosion cracking and corrosion fatigue of magnesium alloys for biodegradable implant applications. JOM 67 (5), 1143–1153.
Jafari, Sajjad, Raman, R.K. Singh, Davies, Chris H.J., 2015c. Corrosion fatigue of a magnesium alloy in modified simulated body fluid. Eng. Fract. Mech. 137, 2–11.
Jafarzadeh, Siavash, Chen, Ziguang, Bobaru, Florin, 2019. Computational modeling of pitting corrosion. Corros. Rev. 37 (5), 419–439.
Jang, Yongseok, Collins, Boyce, Sankar, Jagannathan, Yun, Yeoheung, 2013. Effect of biologically relevant ions on the corrosion products formed on alloy AZ31B: an improved understanding of magnesium corrosion. Acta Biomater. 9 (10), 8761–8770.
Kamrani, Sepideh, Fleck, Claudia, 2019. Biodegradable magnesium alloys as temporary orthopaedic implants: a review. Biometals : Int. J. Role Metal Ions Biol. Biochem. Med. 32 (2), 185–193.
Karma, Alain, Kessler, David A., Levine, Herbert, 2001. Phase-field model of mode III dynamic fracture. Phys. Rev. Lett. 87 (4), 045501.
Kim, Seong Gyoon, Kim, Won Tae, Suzuki, Toshio, 1999. Phase-field model for binary alloys. Phys. Rev. E 60 (6), 7186.
Kondori, B., Benzerga, A.A., 2017. Modeling damage accumulation to fracture in a magnesium-rare earth alloy. Acta Mater. 124, 225–236.
Kovacevic, Sasa, Ali, Wahaaj, Martínez-Pañeda, Emilio, LLorca, Javier, 2023. Phase-field modeling of pitting and mechanically-assisted corrosion of Mg alloys for biomedical applications. Acta Biomater..

Kristensen, Philip K., Niordson, Christian F., Martínez-Pañeda, Emilio, 2020. A phase field model for elastic-gradient-plastic solids undergoing hydrogen embrittlement. J. Mech. Phys. Solids 143, 104093.
Kristensen, Philip K., Niordson, Christian F., Martínez-Pañeda, Emilio, 2021. An assessment of phase field fracture: crack initiation and growth. Phil. Trans. R. Soc. A 379 (2203), 20210021.
Kuhn, Charlotte, Schlüter, Alexander, Müller, Ralf, 2015. On degradation functions in phase field fracture models. Comput. Mater. Sci. 108, 374–384.
Lemkul, Justin A., MacKerell, Jr., Alexander D., 2016. Balancing the interactions of Mg2+ in aqueous solution and with nucleic acid moieties for a polarizable force field based on the classical drude oscillator model. J. Phys. Chem. B 120 (44), 11436–11448.
Lin, Chen, Ruan, Haihui, 2021. Phase-field modeling of mechano–chemical-coupled stress-corrosion cracking. Electrochim. Acta 395, 139196.
Lindström, Rakel, Johansson, Lars-Gunnar, Thompson, George E., Skeldon, Peter, Svensson, Jan-Erik, 2004. Corrosion of magnesium in humid air. Corros. Sci. 46 (5), 1141–1158.
Liu, Z.Y., Li, X.G., Du, C.W., Cheng, Y.F., 2009. Local additional potential model for effect of strain rate on SCC of pipeline steel in an acidic soil solution. Corros. Sci. 51 (12), 2863–2871.
Liu, Chenglong, Xin, Yunchang, Tian, Xiubo, Chu, Paul K., 2007. Degradation susceptibility of surgical magnesium alloy in artificial biological fluid containing albumin. J. Mater. Res. 22 (7), 1806–1814.
Logan, Hugh L., 1958. Mechanism of stress-corrosion cracking in the AZ31B magnesium alloy. J. Res. Natl. Bur. Stand. 61 (6).
Ma, Songyun, Scheider, Ingo, Bargmann, Swantje, 2016. Anisotropic constitutive model incorporating multiple damage mechanisms for multiscale simulation of dental enamel. J. Mech. Behav. Biomed. Mater. 62, 515–533.
Ma, Songyun, Yuan, Huang, 2015. Computational investigation of multi-axial damage modeling for porous sintered metals with experimental verification. Eng. Fract. Mech. 149, 89–110.
Ma, Songyun, Zhou, Bei, Markert, Bernd, 2018. Numerical simulation of the tissue differentiation and corrosion process of biodegradable magnesium implants during bone fracture healing. ZAMM-J. Appl. Math. Mech. (Z. Angew. Math. Mech.) 98 (12), 2223–2238.
Mai, Weijie, Soghrati, Soheil, 2017. A phase field model for simulating the stress corrosion cracking initiated from pits. Corros. Sci. 125, 87–98.
Mai, Weijie, Soghrati, Soheil, Buchheit, Rudolph G., 2016. A phase field model for simulating the pitting corrosion. Corros. Sci. 110, 157–166.
Martínez-Pañeda, Emilio, Golahmar, Alireza, Niordson, Christian F., 2018. A phase field formulation for hydrogen assisted cracking. Comput. Methods Appl. Mech. Engrg. 342, 742–761.
Miehe, Christian, Hofacker, Martina, Welschinger, Fabian, 2010. A phase field model for rate-independent crack propagation: Robust algorithmic implementation based on operator splits. Comput. Methods Appl. Mech. Engrg. 199 (45–48), 2765–2778.
Miehe, Christian, Mauthe, Steffen, Ulmer, H., 2014. Formulation and numerical exploitation of mixed variational principles for coupled problems of cahn–hilliard-type and standard diffusion in elastic solids. Internat. J. Numer. Methods Engrg. 99 (10), 737–762.
Miehe, C., Teichtmeister, S., Aldakheel, F., 2016. Phase-field modelling of ductile fracture: a variational gradient-extended plasticity-damage theory and its micromorphic regularization. Phil. Trans. R. Soc. A 374 (2066), 20150170.
Nachtsheim, Julia, Burja, Jaka, Ma, Songyun, Markert, Bernd, 2022. Long-term in vitro corrosion of biodegradable WE43 magnesium alloy in DMEM. Metals 12 (12), 2062.
Nachtsheim, J., Ma, S., Burja, J., Markert, B., 2024. In vitro evaluation of stress corrosion cracking susceptibility of PEO-coated rare-earth magnesium alloy WE43. Surf. Coat. Technol. 130391.
Naterer, Greg F., Tokarz, C.D., Avsec, Jurij, 2006. Fuel cell entropy production with ohmic heating and diffusive polarization. Int. J. Heat Mass Transfer 49 (15–16), 2673–2683.
Nguyen, Thanh Tung, Bolivar, J., Shi, Y., Réthoré, Julien, King, A., Fregonese, Marion, Adrien, J., Buffiere, Jean-Yves, Baietto, Marie-Christine, 2018. A phase field method for modeling anodic dissolution induced stress corrosion crack propagation. Corros. Sci. 132, 146–160.
Niinomi, Mitsuo, Nakai, Masaaki, Hieda, Junko, 2012. Development of new metallic alloys for biomedical applications. Acta Biomater. 8 (11), 3888–3903.
Prabhu, Deepa B., Dhamotharan, S., Sathishkumar, G., Gopalakrishnan, P., Ravi, K.R., 2018. Stress corrosion cracking of biodegradable Mg-4Zn alloy in simulated body fluid at different strain rates–A fractographic investigation. Mater. Sci. Eng. A 730, 223–231.
Rohanová, Dana, Boccaccini, Aldo Roberto, Horkavcová, Diana, Bozděchová, Pavlína, Bezdička, Petr, Častorálová, Markéta, 2014. Is non-buffered DMEM solution a suitable medium for in vitro bioactivity tests? J. Mater. Chem. B 2 (31), 5068–5076.
Santamaria, M., Di Quarto, F., Zanna, S., Marcus, P., 2007. Initial surface film on magnesium metal: A characterization by X-ray photoelectron spectroscopy (XPS) and photocurrent spectroscopy (PCS). Electrochim. Acta 53 (3), 1314–1324.
Sanz-Herrera, José Antonio, Reina-Romo, Esther, Boccaccini, Aldo R., 2018. In silico design of magnesium implants: Macroscopic modeling. J. Mech. Behav. Biomed. Mater. 79, 181–188.
Scheiner, Stefan, Hellmich, Christian, 2007. Stable pitting corrosion of stainless steel as diffusion-controlled dissolution process with a sharp moving electrode boundary. Corros. Sci. 49 (2), 319–346.
Shen, Zhenquan, Zhao, Ming, Bian, Dong, Shen, Danni, Zhou, Xiaochen, Liu, Jianing, Liu, Yang, Guo, Hui, Zheng, Yufeng, 2019. Predicting the degradation behavior of magnesium alloys with a diffusion-based theoretical model and in vitro corrosion testing. J. Mater. Sci. Technol. 35 (7), 1393–1402.
Ståhle, Per, Hansen, Eskil, 2015. Phase field modelling of stress corrosion. Eng. Fail. Anal. 47, 241–251.
Staiger, Mark P., Pietak, Alexis M., Huadmai, Jerawala, Dias, George, 2006. Magnesium and its alloys as orthopedic biomaterials: a review. Biomaterials 27 (9), 1728–1734.
Sun, Wen, Liu, Guichang, Wang, Lida, Wu, Tingting, Liu, Yang, 2013. An arbitrary Lagrangian–Eulerian model for studying the influences of corrosion product deposition on bimetallic corrosion. J. Solid State Electrochem. 17, 829–840.
Törne, Karin Beaussant, Khan, Fareed Ashraf, Örnberg, Andreas, Weissenrieder, Jonas, 2017. Zn–Mg and Zn–Ag degradation mechanism under biologically relevant conditions. Surf. Innov. 6 (1–2), 81–92.
Wagener, V., Virtanen, S., 2016. Protective layer formation on magnesium in cell culture medium. Mater. Sci. Eng. C 63, 341–351.
Wei, Liangyu, Gao, Ziyuan, 2023. Recent research advances on corrosion mechanism and protection, and novel coating materials of magnesium alloys: a review. RSC Adv. 13 (12), 8427–8463.
Winzer, Nicholas, Atrens, Andrej, Song, Guangling, Ghali, Edward, Dietzel, Wolfgang, Kainer, Karl Ulrich, Hort, Norbert, Blawert, Carsten, 2005. A critical review of the stress corrosion cracking (SCC) of magnesium alloys. Adv. Eng. Mater. 7 (8), 659–693.
Wu, Tao, De Lorenzis, Laura, 2016. A phase-field approach to fracture coupled with diffusion. Comput. Methods Appl. Mech. Engrg. 312, 196–223.
Xie, Chao, Bai, Shijie, Liu, Xiao, Zhang, Minghua, Du, Jianke, 2022. Stress-corrosion coupled damage localization induced by secondary phases in bio-degradable Mg alloys: phase-field modeling. J. Magnes. Alloys.
Xin, Yunchang, Huo, Kaifu, Tao, Hu, Tang, Guoyi, Chu, Paul K., 2008. Influence of aggressive ions on the degradation behavior of biomedical magnesium alloy in physiological environment. Acta Biomater. 4 (6).
Yang, Miao, Liu, Xiaobo, Zhang, Zhiyi, Song, Yulai, 2019. Stress corrosion behavior of AM50gd magnesium alloy in different environments. Metals 9 (5), 616.
Yavuzyegit, Berzah, Karali, Aikaterina, De Mori, Arianna, Smith, Nigel, Usov, Sergey, Shashkov, Pavel, Bonithon, Roxane, Blunn, Gordon, 2024. Evaluation of corrosion performance of AZ31 Mg alloy in physiological and highly corrosive solutions. ACS Appl. Bio Mater..
Zeller-Plumhoff, Berit, AlBaraghtheh, Tamadur, Höche, Daniel, Willumeit-Römer, Regine, 2022. Computational modelling of magnesium degradation in simulated body fluid under physiological conditions. J. Magnes. Alloys 10 (4), 965–978.
Zhang, Xiaoxuan, Krischok, Andreas, Linder, Christian, 2016. A variational framework to model diffusion induced large plastic deformation and phase field fracture during initial two-phase lithiation of silicon electrodes. Comput. Methods Appl. Mech. Engrg. 312, 51–77.
Zhou, Bei, Heider, Yousef, Ma, Songyun, Markert, Bernd, 2019. Phase-field-based modelling of the gelation process of biopolymer droplets in 3D bioprinting. Comput. Mech. 63, 1187–1202.